THESIS FOR THE DEGREE OF
DOCTOR OF PHILOSOPHY

Neutron scattering for sustainable energy materials: investigations of proton dynamics in acceptor doped barium zirconates

Daria Noferini

Department of Physics

CHALMERS UNIVERSITY OF TECHNOLOGY

Göteborg, Sweden 2018

Neutron scattering for sustainable energy materials: investigations of proton dynamics in acceptor doped barium zirconates

Daria Noferini

ISBN 978-91-7597-709-6

Doktorsavhandlingar vid Chalmers Tekniska Högskola

Ny serie nr 4390

ISSN 0346-718X

Department of Physics

Chalmers University of Technology

SE-412 96 Göteborg, Sweden

This thesis project has been primarily financially supported by grants from the Swedish Research Council (grant No. 2010-3519 and 2011-4887) and from the Institut Laue-Langevin, Grenoble, France (grant No. ILL1279.1).

Cover:

Artistic view of proton motions in a perovskite material.

Chalmers Reproservice

Göteborg, Sweden 2018

Neutron scattering for sustainable energy materials: investigations of proton dynamics in acceptor doped barium zirconates

Daria Noferini
Department of Physics
Chalmers University of Technology

Abstract

Proton conducting oxides are currently receiving considerable attention for their present or potential use as electrolytes in technological devices such as sensors and electrolysers and, in particular, solid oxide fuel cells, which are among the most promising apparatuses for energy conversion. One of the main challenges for these latter devices is to combine the advantages of a solid electrolyte with those of operational temperatures below 750 °C, which is currently hampered by insufficient conductivities in the targeted temperature range. The development of new electrolytes meeting the requirements for applications depends on a better understanding of the physico-chemical processes underlying ionic conductivity in these materials. Towards this aim, this thesis reports on investigations of key properties in hydrated samples of the perovskites $BaZr_{0.9}M_{0.1}O_{2.95}$ with M = Y and Sc and $BaZr_{1-x}In_xO_{3-x/2}$ with x = 0.1–0.275, well-known and promising proton conducting oxides. Of specific concern in this thesis is the study of the effect of the type (M) and concentration (x) of dopant atoms on the atomic-scale proton dynamics over a wide time-range, from picoseconds to nanoseconds, using different state-of-the-art neutron scattering techniques at the neutron scattering facilities Institut Laue-Langevin in Grenoble, France, and Forschungs-Neutronenquelle Heinz Maier-Leibnitz in Garching, Germany. The results show a complex dynamics, arising from a distribution of different proton sites, a consequence of a disordered structure of the materials. Analysis of the short time scale dynamics discloses localized dynamics interpretable as proton jumps and reorientations of the hydroxyl groups. Faster local motions are observed in more distorted structures associated with higher doping levels, whereas no substantial differences are observed for different dopant ions. Analysis of the long time scale dynamics reveals long-range diffusion of protons, which can be described as a jump-diffusion process. Higher dopant concentrations lead to higher activation energies, still well below those for macroscopic proton conductivities, but larger fractions of mobile protons. This new insight adds to the previous knowledge of proton dynamics in perovskite materials and can be useful to develop strategies for the design of improved proton conductors for technological applications.

Keywords: *Proton conductors, perovskites, proton dynamics, neutron scattering, QENS, fuel cells, energy materials*

Acknowledgments

Supervisors:

Maths Karlsson

Chalmers University of Technology, Göteborg

and

Michael M. Koza

Institut Laue-Langevin, Grenoble.

❋ ❋ ❋

Seikh M. H. Rahman, Sten Eriksson Göran Wahnström, Laura Mazzei,

Carin Österberg, and Ezio Zanghellini;

Aleksandar Matic, Lena Falk, and Anna Lindqvist.

Chalmers University of Technology, Göteborg.

Peter Fouquet, Bernhard Frick, Andrew Wildes, Ingo Hoffmann,

Jacques Ollivier, Bela Farago, Richard Ammer, Markus Appel,

Didier Richards, Eric Thaveron, Dimitry Renzy, Wayne Clancy,

Jerome Halbwachs, Claude Gomez;

Helmut Schober, William G. Stirling, Mark R. Johnson, and Laurence Tellier.

Institut Laue-Langevin, Grenoble.

Gøran J. Nilsen.

ISIS Facility, STFC Rutherford Appleton Laboratory, Didcot.

Marco Maccarini.

Université Grenoble Alpes, Grenoble.

Wiebke Lohstroh and Zachary Evenson.

Heinz Maier-Leibnitz Zentrum, Technische Universität München, Garching.

Moureen C. Kemei.

University of California, Santa Barbara.

❋ ❋ ❋

I wish to extend my gratitude to all those people who supported me
in this “journey”.

"But I don't want to go among mad people," Alice remarked.
"Oh, you can't help that,", said the Cat:
"we're all mad here, I'm mad. You're mad.
"How do you know I'm mad?" said Alice.
"You must be," said the Cat, "or you wouldn't have come here."
Lewis Carroll, Alice's Adventures in Wonderland

To all the curious people

Contents

List of appended papers

I. Proton Dynamics in Hydrated $BaZr_{0.9}M_{0.1}O_{2.95}$ (M = Y and Sc) Investigated with Neutron Spin-Echo.

Daria Noferini, Michael M. Koza, Peter Fouquet, Gøran J. Nilsen, Moureen C. Kemei, Seikh M. H. Rahman, Marco Maccarini, Sten Eriksson, and Maths Karlsson.

J. Phys. Chem. C **120**, 13963 (2016).

II. Localized Proton Motions in Acceptor-Doped Barium Zirconates.

Daria Noferini, Michael M. Koza, and Maths Karlsson.

J. Phys. Chem. C **121**, 7088 (2017).

III. Study of the Hydration Level in Proton Conducting Oxides Using Neutron Diffraction with Polarization Analysis.

Daria Noferini, Michael M. Koza, Gøran J. Nilsen, and Maths Karlsson.

Under review.

IV. Role of the Doping Level on Localized Proton Motions in Acceptor-Doped Barium Zirconate Proton Conductors.

Daria Noferini, Michael M. Koza, Seikh M. H. Rahman, Zach Evenson, Gøran J. Nilsen, Sten Eriksson, Andrew R. Wildes, and Maths Karlsson.

Phys. Chem. Chem. Phys. (2018) DOI: 10.1039/c7cp07340b.

V. Proton Jump Diffusion Dynamics in Hydrated Barium Zirconates Studied by High-Resolution Neutron Backscattering Spectroscopy.
Daria Noferini, Bernhard Frick, Michael M. Koza, and Maths Karlsson.
Under review.

Contribution report

I co-proposed/proposed the neutron experiments (Papers I–V), and carried out the neutron scattering experiments (Papers I–V) and the infrared measurements (Paper I). I analysed the data of the neutron scattering (Paper I–V), infrared spectroscopy (Paper I), and thermogravimetric analysis experiments (Papers I and III). I wrote the first drafts, further developing the manuscripts together with M. K. and M. M. K.

Foreword

This thesis reports on investigations of proton dynamics in proton conducting oxides, namely hydrated acceptor doped barium zirconate based oxides with perovskite structure, by means of neutron scattering. The project has been undertaken as a collaboration between Chalmers University of Technology and the Institut Laue-Langevin (ILL, Grenoble, France). The latter is an international research centre and neutron source at the leading edge of neutron research.

Proton conduction is an exciting phenomenon studied already in the beginning of the 19th century and at the basis of several fundamental processes transversally crossing different fields from biology to the most recent technological developments, as introduced in Chapter 1. The increasing need for sustainable energy-related technologies in modern times directs materials research to strive towards their constant improvement. A relevant example is the effort to lower the operational temperatures of solid oxide fuel cells in order to combine the currently achieved advantages given by the solid oxide electrolyte in high-temperature fuel cells with improved durabilities, reduced costs and rapid operations. A promising strategy for this goal is to substitute the traditional electrolytes based on oxygen ion transport with proton conducting oxides. These aspects are detailed in Section 1.2. Among the many different oxides showing proton conductivity, *cfr* Chapter 2, perovskite oxides and in particular barium zirconates currently represent one of the best compromises among the properties needed in fuel cells such as chemical stability and high ionic conductivity. More

details about this are given in Section 2.1. Although the conductivity values are below the threshold for applications at low temperatures, deeply understanding the proton conduction mechanisms in these promising materials represents a fundamental step in the tailoring of new improved proton conductors. There is a general agreement on a Grotthuss-like mechanism for proton diffusion in perovskite oxides. The Grotthuss mechanism is introduced together with its main alternative, the vehicle mechanism, in Section 1.1, and more information is then given in Section 2.1.3. In brief, protons are supposed to transfer (jump) between neighbouring oxygens with reorientations of -OH groups in between such transfers. The repetition of these steps leads to long-range proton diffusion. However, the very details of such a mechanism are yet not (completely) disentangled, as explained in Section 2.1.3. One of the main open points regards the effect of the acceptor doping on the proton dynamics at the atomic level. The acceptor doping (*cfr* Section 2.1.2), for example the substitution of some Zr^{4+} with the same amount of Ga^{3+} in barium zirconates, creates oxygen vacancies thus enabling the incorporation of protons during hydration. Nevertheless, the effect of the acceptor doping is not just to enhance the concentration of protons, but depending on the type and concentration of the substituting cation it may have a strong impact on the proton conductivity. With a focus on this aspect, samples were chosen in order to investigate the effect of doping/hydration level and different dopants on both the localized dynamics and long-range proton diffusion. The studies hence focus onto a series of 10% Y-, In- and Sc-doped samples, and onto a series of In-doped samples with doping level ranging from 0 to 27.5%, as detailed in Section 2.2. The primary tools to this aim comprised a combination of several neutron scattering techniques, complemented by infrared spectroscopy, thermogravimetric analysis, x-ray diffraction, scanning electron microscopy, and energy dispersive x-ray analysis. Neutron scattering, and notably quasielastic neutron scattering, emerged among the different experimental techniques due to

the unique features of neutrons as a probe, including a high sensitivity for hydrogen. A short introduction to the technique is given in Chapter 3. Moreover, different instrumental techniques and setups enable the exploration of different length-time regions, therefore allowing to focus on different dynamical processes, as explained in Chapter 4. The results, summarised in Chapter 5, point towards a complex dynamics, arising from the presence of different proton sites (*cfr* Papers I–III and V). Its onset was also determined with unprecedented accuracy as a function of temperature, dopant concentration and type of dopant atom (*cfr* Paper V). The localized dynamics, possibly dominated by -OH reorientations, seems to vary as a function of local distortions induced by the dopant (*cfr* Papers II–IV). Also the long-range diffusion was identified and successfully modelled as a Chudley-Elliot jump-diffusion mechanism with a characteristic jump distance of 3 Å, increased activation energy as a function of doping concentration, and diffusion coefficients at 550 K of the order of 10^{-7} cm^2/s (*cfr* Paper V). These new insights improve our understanding of the proton conduction mechanism in perovskite materials, which is at the basis of the rational design of new proton conductors with optimized conductivity. Further, this thesis also disclosed some new questions, paving the road for further experiments and possible perspectives (*cfr* Chapter 6).

Chapter 1

Proton conduction: background and motivations

Proton conduction plays an essential role in a variety of processes in diverse fields from biology, such as in proton pumps in several organisms including humans or photosynthesis in green plants, to advanced technology in devices such as electrochromic displays, sensors, electrolysers and hydrogen fuel cells [1–5]. Even limiting the focus onto the technological applications,[1] the materials showing proton conductivity are numerous and various, and an extensive survey is beyond the scope of this thesis. However, in the following it will be given a brief selection of materials belonging to different classes and being important either historically or in relation to the main application presented here, *i.e.* fuel cells, with the aim to illustrate the wide range of the field.

Many milestones in the field of proton conduction have water containing systems in leading roles [4, 6]. The existence of protons in aqueous solutions was already conjectured by de Grotthuss in the beginning of the 19th century

[1] Since the proton-transport phenomena in the mentioned technological devices are close to the thermodynamic equilibrium [4], the considerations in the following will be limited to this case.

in his publication *"Mémoire sur la décomposition de l'eau et des corps qu'elle tient en dissolution à l'aide de l'électricité Galvanique"* [7], and at the end of the same century ice was the first solid material for which proton conduction was studied [4, 6]. The hydrated perfluorinated sulfonated polymer NAFION, commercialized by DuPont in the late 1960s and used as a membrane for fuel cells in the Gemini and Apollo space programs, was the first proton conducting material to be used in applications [4, 6]. Similar hydrated materials interesting for technological applications due to the good conductivities and chemical stability are sulfonated polybenzimidazole (S-PBI) and sulfonated polyether ether ketone (S-PEEK) [8]. These polymers have conductivity values of the order of 10^{-2}–10^{-1} S/cm at room temperature [8, 9], *i.e.* in the range required for the above-mentioned devices. Their applicability is however limited to the low temperatures, below *ca* 100 °C, although the use of composite materials seems to be encouraging in enabling higher operational temperatures [8]. The first solid materials showing relevant proton conductivity (of the order of 10^{-3} S/cm at room temperature [10]) were again water containing systems: the layered compound HUP and HUAs, having formula $H_3OUO_2XO_4{\cdot}3H_2O$, with X= P and X= As, respectively [4, 6].

Other inorganic solids showing promising conductivities at moderate temperatures (120–250 °C) are solid acid compounds, such as $CsHSO_4$ and CsH_2PO_4. The typical structure of this kind of materials is formed by oxyanions, XO_4 (*e.g.* SO_4 or PO_4), linked together by hydrogen bonds. In comparison with water containing systems they offer the advantages for applications of anhydrous proton transport and temperature stability up to *ca* 250 °C [11].

Remaining in the domain of solid materials, densely packed oxides constitute a large group of proton conductors, comprising a series of different classes of materials. Together with high conductivity values, their main advantages are stability and durability, even at high temperatures around 1000 °C. They are at

the heart of solid oxide fuell cells (SOFCs). Achieving high conductivities and chemical and mechanical stability at temperatures below 750 °C are the main challenge for these materials [3, 4, 6, 8, 12, 13]. Yet, reaching these goals would enable several improvements in applications, as it will be detailed below.

1.1 Proton conduction mechanisms

There are two principal mechanisms that describe proton diffusion without requiring even the momentary existence of free protons, *i.e.* in which the proton is constantly shielded by some electron density during its entire diffusion path [4]. In the first one, the *vehicle mechanism* [14], Figure 1.1 a), proton migration is assisted by the translational dynamics of bigger chemical species. The proton diffuses with such "vehicles", for example as H_3O^+, while the net transport of protons is enabled by the counter diffusion of the unprotonated vehicles (H_2O in the former example). The proton conductivity is therefore regulated by the rate of the molecular diffusion of the vehicles. In the second one, the *Grotthuss mechanism* [7], Figure 1.1 b), the sorrounding ions (hosts) have pronounced local dynamics but reside on their sites, and the protons are transferred within hydrogen bonds from one host to another, *i.e.* they site-to-site hop between proton donor and proton acceptor sites, with local reconstruction of the atomic environment around the moving protons, such as reorientation of individual species or more extended ensembles. The relevant rates for the Grotthuss mechanism are hence those of proton transfer and reorganization of its environment. The two mechanisms may even coexist in a certain compound, generally switching from Grotthuss to vehicle with increasing temperature [4].

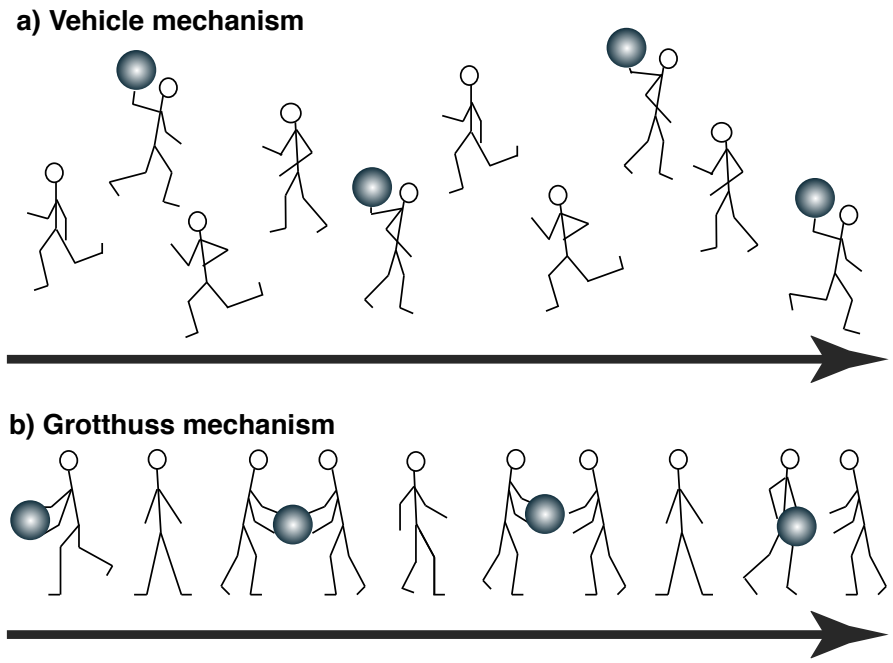

Figure 1.1: Sketch of a) vehicle and b) Grotthuss mechanisms for proton conduction.

1.2 Proton conducting SOFCs

The increasing trend for world energy consuption[2] makes sustainable technologies for energy conversion more and more essential. Within the currently available technologies, fuel cells enable to directly convert stored chemical energy from a fuel into usable electrical energy with high efficiency, also reducing, or even eliminating, harmful emissions [16, 17].

Fuel cells can be regarded as a cross between a battery and a continuously fuelled, air breathing, device [18, 19]. They were invented in the middle of the 19th century by sir William Grove and had one of the first successful applications within the space technologies, for which an electrical energy conversion device also capable of providing heat and potable water was a convenient improvement

[2]The U.S. Energy Information Administration (EIA) estimates a 48% growth between 2012 and 2040 [15].

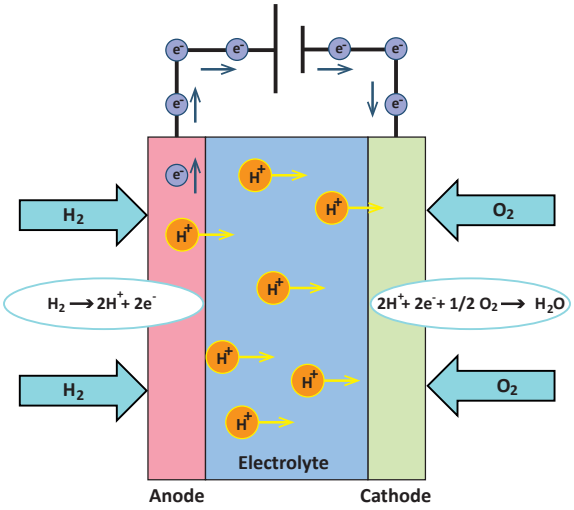

Figure 1.2: Schematic view of a SOFC based on a proton conducting electrolyte

in comparison with other power sources, such as batteries [6, 19].

A fuel cell is composed by a pair of electrodes at the two sides of an ion-conducting material (electrolyte). An oxidant, usually oxygen in the form of air, is fed to the cathode, and fuel is supplied to the anode. The type of electrolyte is commonly used to classify different types of fuel cells. When a solid oxide electrolyte is employed, fuel cells, termed in this case SOFCs, are extremely versatile, being capable to oxidise a wide range of fuels such as hydrogen, hydrocarbons or even carbon [16]. The solid electrolyte is usually an oxide ion conductor, but depending on the type of fuel cell it can also be a proton, carbonate or hydroxide ion conductor [18]. A scheme of functioning of a SOFC based on a proton conducting electrolyte is shown in Figure 1.2.

The most commonly used SOFCs, based on oxygen ion transport, normally operate in a temperature range of around 800–1000 °C. Drawbacks of this high temperature include high cell costs, limited endurance, and long start up and shutdown cycles, which reduce the applicability of SOFCs in portable power and transportation devices [16–18]. Although there is not an ideal operational temperature for fuel cells in general, it is estimated that lowering that of SOFCs

below 650 °C would increase the life-time up to more than ten years, increase the maximum theoretical efficiency [16], and sensibly reduce the time needed for start up, therefore unlocking a wide range of new potential applications [16–18]. Not surprisingly, thus, a large part of solid-state materials research is devoted to the improvement of the materials composing SOFCs in order to enable their functioning at lower operational temperatures [17]. With respect to the electrolytes, higher conduction at lower temperature is envisaged for proton conducting electrolytes, due to the much smaller size of the proton than the oxide ion [18]. Another advantage of using proton conducting electrolytes is that water, as by-product, is produced at the cathode side instead of at the anode, preventing the dilution of the fuel and minimizing the re-oxidation of the anode [20].

To ensure a sufficiently small total internal resistance (*i.e.* electrolyte plus electrodes) of a SOFC, the target value for the area specific resistivity (ASR) of the electrolyte is set at 0.15 Ω cm^2 [21]. Considering that films of oxide electrolytes can be reliably produced by inexpensive, conventional ceramic fabrication routes having thicknesses down to *ca* 15 μm, it follows that the specific conductivity of the electrolyte must exceed 10^{-2} S/cm [21]. Nevertheless, in the operational temperature range of *ca* 100–750 °C, *i.e.* the one of low and intermediate-temperature SOFCs,[3] currently available materials do not reach this goal [22]. This "electrolyte gap" constitutes one of the main problems to overcome in order to bring low-temperature and intermediate-temperature SOFCs into our everyday life. Fuel cells using solid acids as electrolytes (Solid Acid Fuell Cells, SAFCs), which operate around 200–250 °C, can be considered as an interesting alternative to low-temperature SOFCs [11, 23, 24]. However,

[3]On the basis of their operational temperature, fuel cells can be also classified into high-, intermediate- and low-temperature ones. Although their ranges are not universally defined, they indicatively take values of T>750 °C, 500 °C<T<750 °C, and T<500 °C, respectively [18, 21].

this relatively young technology presents some disadvantages, deriving for example from solubility in water of the electrolyte, weak mechanical properties, the need of a high load of expensive Pt electrocatalyst, the limited operational temperature range, and the need for many electrolytes of a (minimum) level of hydration to prevent decomposition and to enable the superprotonic phase transition at elevated temperatures [24]. However, the use of composite materials as electrolytes or Pt decorated carbon nanotubes as electrodes are recently tested strategies to overcome some of the above mentioned limitations [24, 25].

Chapter 2

Proton conducting oxides

To be successfully applied as electrolyte in proton conducting SOFCs and other important devices such as sensors and electrolyser, a proton conducting material is usually required to show a balance among high proton concentration (*i.e.* a favourable hydration kinetics), high proton mobility, chemical stability, and good mechanical properties.

First observations and speculations regarding hydrogen in oxides are dated back to the 1950s and 1960s [26, 27]. In 1972, predominant proton conductivity was observed for the first time in a fluorite-related oxide (general formula MO_2, where M is a tetravalent cation), namely acceptor doped thoria (ThO_2) at high temperatures, high hydrogen partial pressure and low oxygen partial pressure [4, 28]. Since then, several materials have been investigated, and a broad range of oxides have shown proton conducting properties [3, 13, 29]. For example, remaining in the group of fluorite-related oxides, which are commonly used as electrolyte in oxide ion SOFCs, whereas when M is Zr, Hf or Ce the proton conductivity is almost negligible in respect to oxide ion conductivity, due to a poor solubility of the protons, rutile TiO_2 shows significant proton conductivity (of the order of 10^{-5} S/cm at 800 °C for undoped TiO_2) [13, 30].

La_6WO_{12} is another example of a fluorite-related oxide that shows considerable proton conductivity, with a maximum of the order of 10^{-3} S/cm in a wet hydrogen atmosphere at 750 °C [6, 31]. Conversely, spinels (AB_2O_4) seem to do not present proton conductivity, possibly as a consequence of a too rigid oxide ion sublattice [6]. Proton conductivity was reported in the 1990s for the phosphate $LaPO_4$. For this compound, a low solubility of the protons limits the achievable conductivity. More recently, diphosphates of tetravalent metals such as SnP_2O_7 received attention because of a very high proton conductivity, exceeding 0.1 S/cm around a temperature of 200 °C [32]. However, the initial enthusiasm decreased after evidences that the observed enhanced conductivity is likely due to remaining phosphoric acid [33]. Proton conducting oxides with a similar structure to $LaPO_4$ are rare-earth orthoniobates and orthotantalates (RMO_4 with R=La, Gd, Nd, Tb, Er or Y and M = Nb or Ta). Although their conductivities (10^{-3} S/cm at 800 °C) are not exceptional compared with other oxides, these materials are interesting because of a high stability in CO_2 atmosphere [6, 34]. Also rare-earth oxides (R_2O_3) such as Er_2O_3 showed proton conductivity, although mainly in the high-temperature range [35]. Similarly to orthoniobates and orthotantalates, pyrochlore-type oxides ($A_2B_2O_6X$, with A being an alkali ion, B a tranistion element and X= F, O or OH) are considered for applications due to their high stability towards CO_2 and H_2O. The associated proton conductivity values are of the order of 10^{-3} S/cm at 800 °C and are significant mainly in the high-temperature range [36]. In the 1980s, Takahashi and Iwahara reported on proton conduction in the oxides with perovskite structure (ABO_3) with composition $LaYO_3$ and $SrZrO_3$ [37]. Since these pioneering studies, and despite the many different structure-types tested in the last 45 years, the perovskite structure seems to be the most favourable for the requirements needed for applications. High values of conductivities are shown by many different materials of this class, and particularly by systems presenting cubic or slightly

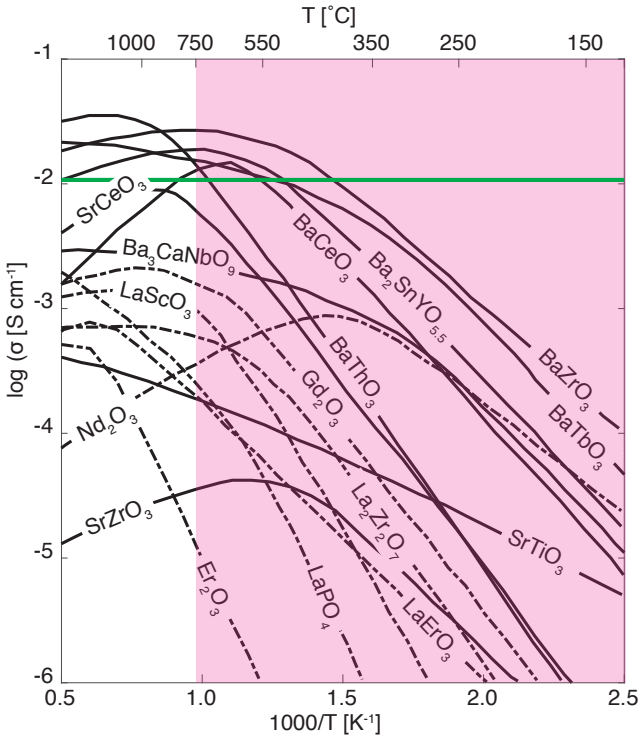

Figure 2.1: Proton conductivity values for different oxides derived from proton concentration and mobilities, as reported in Ref. [3]. The range of interest of low- and intermediate-temperature SOFCs is highlighted by the pink background. Perovskite-type oxides are shown as solid lines, as opposed to dashed lines for materials having different structure-types. Conductivity values needed for applications are underlined by a green solid line.

reduced symmetry [6, 13]. For example, proton conductivity exceeds 10^{-2} S/cm at 800 °C in orthorhombic barium cerates [38]. Perovskite oxides generally support relatively high temperatures and low humidity, but mechanical and chemical stability are the major issues concerning these materials [6, 13]. Proton conduction was also observed in brownmillerite oxides ($A_2B_2O_5$), which can be seen as oxygen-deficient perovskites with ordered oxygen vacancies [6, 13, 39]. $Ba_2In_2O_5$ hydrates to its oxyhydroxide form $Ba_2In_2O_4(OH)_2$ around 300 °C in a humid atmosphere [6,13,39]. The advantage of brownmillerite oxides is mainly the high proton content that can be achieved, whereas the main problems are caused by reactions with humidity and CO_2 [13, 40].

Figure 2.1 shows the proton conductivity values for different oxides expected on the basis of data on proton concentration and mobilities [3]. It is possible to note that several perovskite-type oxides reach good values of conductivity even in the low- and intermediate-temperature regions. The high interest for these materials in respect to next generation SOFCs is therefore comprehensible. However, although the conductivity values, especially at low temperatures, are yet too low compared with those required for applications (10^{-2} S/cm [21]), understanding the details of the proton conduction mechanism in the most promising materials is considered to be important for the further development of electrolytes.

2.1 Proton conducting perovskites

2.1.1 Overview and general structure

The term *perovskite* originally identifies a calcium titanate mineral, named after the Russian mineralogist Lev Perovski [41]. In a more general way, it is used to refer to a wide class of compounds with general formula ABX_3, where A and B are cations, with A larger than B, and X is an anion, often oxygen. Figure 2.2 shows the ideal perovskite structure: the A cations are arranged in a cubic symmetry; the X anions, at the centre of each face of the cube, form an octahedron, with the B cation at its centre. However, depending on the relative sizes of A and B, distortions away from cubic symmetry can occur. The Goldschmidt factor t [42], defined as $t = \frac{r_A + r_X}{\sqrt{2}(r_B + r_X)}$, where r_A, r_B and r_X are the ionic radii of A, B, and X, respectively, can be used to speculate about possible structures. It is equal to 1 for an ideal cubic structure.

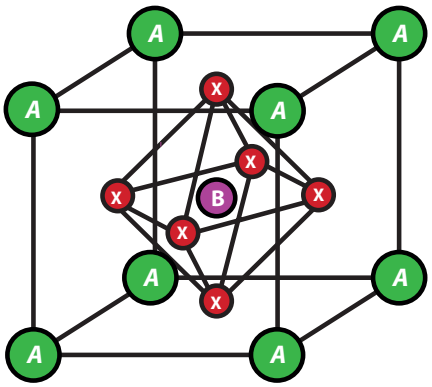

Figure 2.2: Schematic view of the ideal cubic perovskite structure, with general formula ABX_3. The cation A is larger than the cation B, X is an anion.

2.1.2 Doping and proton incorporation

As seen in the previous section, protons are not part of the nominal perovskite composition. In wet atmosphere, protons can enter into the perovskite structure as interstitial defects or compensated by metal vacancies [13]. However, to significantly enhance their presence, as needed for applications, a common strategy is to use acceptor doping: lower-valent ions are introduced into the B-site (for example some Y^{3+} substitute the same amount of Zr^{4+}) and are compensated by oxygen vacancies in the dehydrated state [3]. If the material is exposed to water vapour, water molecules from the gaseous phase dissociate into hydroxide ions and protons; the hydroxide ions fill the oxide ion vacancies and the protons form covalent bonds with the lattice oxygens [3]. A schematic view of the doping and hydration processes is sketched in Figure 2.3, for barium zirconate, $BaZrO_3$, as an example. In these compounds, doped with trivalent ions, the oxygen vacancy concentration in the dry state is ideally equal to half of the dopant concentration, and the concentration of protonic defects in a fully hydrated sample matches that of the dopant [3]. Another strategy to incorporate protons is to synthesise cation-offstoichiometric perovskites: quaternary

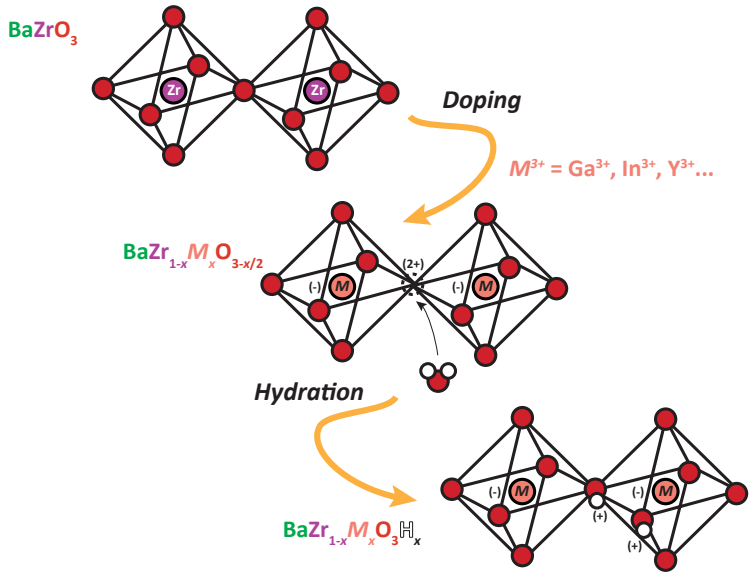

Figure 2.3: Schematic view of the doping and hydration processes for barium zirconate. For clarity reason, the drawing only focuses onto two octahedra, hence also omitting the cubic cages formed by the Ba ions. A lower-valent ion M^{3+} (*e.g.* Y^{3+}, Gd^{3+}...) is inserted into the B-site occupied by Zr^{4+}, creating oxygen vacancies. By exposing the materials to water vapour at high temperatures, water molecules from the gaseous phase dissociate into hydroxide ions and protons; the oxygen vacancies are filled by hydroxide ions, whereas the protons form covalent bonds with oxygens of the perovskite lattice.

perovskite-related structures with general formula $A_2BB'O_6$ and $A_3BB'O_9$ and an excess of lower valent B' cations. The consequent charge imbalance is compensated by protons [2, 3, 13, 43]. A classic example of this class of materials is BCN18 ($Ba_3Ca_{1.18}Nb_{1.82}O_{8.73}$). It has been conjectured that proton mobility would be favoured by this approach [13, 43]. However, the conductivities presented by these materials are not always improved compared with simple perovskites [2, 3].

The hydration/dehydration equilibrium in an acceptor doped solid oxide can

be written in Kröger-Vink notation[1] as:

$$H_2O(g) + V_{\mathrm{O}}^{\bullet\bullet} + O_{\mathrm{O}}^{\times} \rightleftharpoons 2(OH_{\mathrm{O}}^{\bullet}), \tag{2.1}$$

where $V_{\mathrm{O}}^{\bullet\bullet}$ is the oxygen vacancy, $O_{\mathrm{O}}^{\times}$ is the oxide ion, and $OH_{\mathrm{O}}^{\bullet}$ is the hydroxyl ion. Making use of thermodynamic quantities and relations, it is possible to calculate the theoretical concentration of protonic defects as [44]:

$$[\mathrm{OH}_{\mathrm{O}}^{\bullet}] = \mathrm{N_O}\frac{\mathrm{K'}}{\mathrm{K'}-4}\left[1-\sqrt{1-\frac{\mathrm{K'}-4}{\mathrm{K'}}\left(\frac{2[\mathrm{M}]}{\mathrm{N_O}}-\frac{[\mathrm{M}]^2}{\mathrm{N_O^2}}\right)}\right], \tag{2.2}$$

where N_{O} is the number of oxygen sites per formula unit, which is therefore equal to 3 for a perovskite, and $[M]$ is the dopant concentration. $K' = p_w K$, where p_w is the vapour partial pressure and K is the equilibrium constant. The details of the derivation are given in appendix A.1.

The theoretical concentration of protonic defects as a function of temperature in different conditions can be used as a guideline during experimental procedures. Figure 2.4 shows some examples for barium zirconate doped with 10% Sc, Y or In at conditions relevant for the present study. The details of their calculation are given in appendix A.2.

2.1.3 Proton dynamics

After the first evidences [37], more and more studies confirmed proton conductivity in a wide range of perovskite materials, covering all combinations of valence of the A and B cations [13]. For example, proton conduction was reported in acceptor doped II-IV perovskites such as $BaCeO_3$, $BaTbO_3$, $BaZrO_3$, I-V perovskites such as $KTaO_3$, III-III perovskites such as $LaScO_3$ [13]. Gener-

[1] In Kröger-Vink notation, the superscript • indicates a positive effective charge, and the superscript × indicates a neutral effective charge.

ally, the highest values of conductivity are found among II-IV perovskites, and for this reason alkaline earth cerates and zirconates (ACeO$_3$ and AZrO$_3$, respectively, with A= Ca, Sr, or Ba) are among the most studied materials [6, 12, 13]. However, the high basic character of alkaline earth metals makes these proton conductors prone to reactions with CO_2 [13]. Cerates have usually high protonic conductivity because of the high concentration of protonic charge carriers but are also very vulnerable [3, 13]. For instance, both $SrCeO_3$ and $BaCeO_3$ present high values of conductivity as also shown by Figure 2.1. However, they react to carbonates even with low CO_2 levels [3, 45], have only a slight thermodynamical stabizilation with respect to the decomposition into the binary oxides [46], and are not stable in an atmosphere of high humidity, forming alkaline earth hydroxides [47]. Conversely, barium zirconates, still presenting high

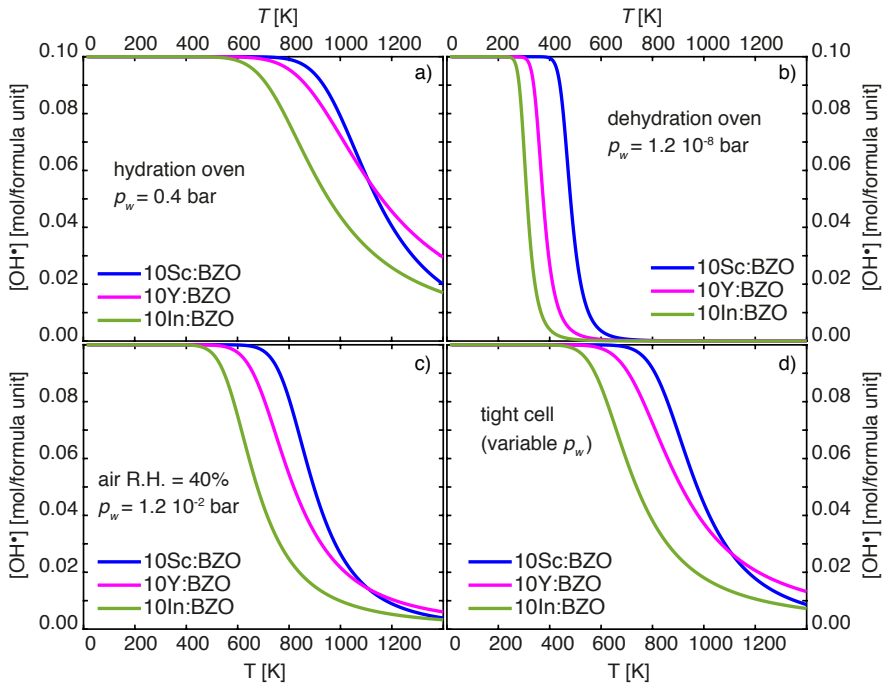

Figure 2.4: Theoretical concentration of protonic defects as a function of temperature for $BaZr_{0.9}M_{0.1}O_3H_{0.1}$ (10M:BZO), with M= Sc, Y and In. The curves are calculated for: a) a hydration procedure; b) a dehydration procedure c) air with 40% relative humidity (R.H.); d) a tightly closed cell.

conductivity values, are chemically more stable and have also better mechanical properties [3, 6, 12]. They are therefore among the best compromise in terms of the properties needed for effective applications.

Regarding the proton conduction mechanism, the first point to address was to discriminate between the vehicle and the Grotthuss mechanisms (*cfr* Section 1.1). Structural reasons would already point towards Grotthuss-type mechanisms, as perovskites are closely packed in respect to oxygen. This would allow oxygen and hydroxyl ions to migrate only *via* vacancies, leading to lower diffusivities than those observed for protonic defects [4]. This was evidenced since the very early studies in the 1980s [48], and later confirmed by different techniques [12, 43, 49, 50], such as ^{18}O-tracer experiments [49] and thermoelectric power measurements [50].

Two elementary steps are supposed to take place within the Grotthuss mechanism: i) proton transfer between neighbouring oxygens, and ii) reorientational motion of the entire hydroxyl group. A schematic representation of the two steps is shown in Figure 2.5. The repetition of these steps gives rise to long-range proton diffusion.

The first step requires the breaking of the O-H covalent bond, whereas such a bond remains intact during the reorientational step, only changing its orientation. The difference in bond energies may suggest the transfer step as the rate-limiting one for proton diffusion. Support on this hypothesis came from various investigations. For example, quantum mechanical dynamics simulations found weak hydrogen bonds and shorter time scale for rotations than transfers [51, 52], and quasielastic neutron scattering (QENS) probed fast dynamics interpreted as fast rotations [53]. However, the reorientational motion involves the breaking of hydrogen bonds, and the strong hydrogen bond interactions, indicated for example by the pronounced red-shifted OH-stretching absorption in the infrared (IR) spectra [54, 55], may conversely suggest that rotation can be the rate-limiting

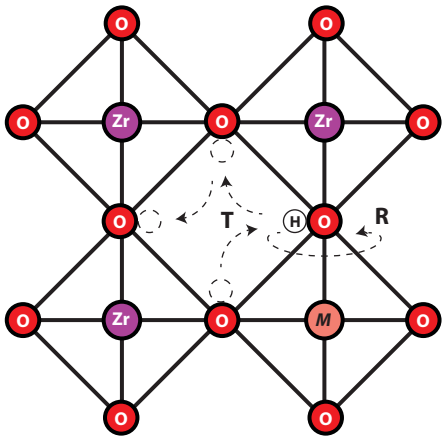

Figure 2.5: Schematic representation of the two elementary steps for proton diffusion in a barium zirconate doped with a generic dopant M: i) proton transfer between neighbouring oxygens (T), and ii) reorientational motion of the OH group (R).

step [13]. Results from computational studies of cubic perovskites hint instead to a similar probability for the two processes to occur [56, 57]. Different investigated systems may lead to different conclusions; yet, even for a certain material an agreement among different studies is not reached. For example, in barium zirconates, computational studies generally concluded that the transfer is the slowest process [52,58,59]. However, quite similar activation energies for the two steps are also reported [57], at least in regions far from the dopant atoms and far from grain boundaries (*i.e.* away from the influence of other possible effects that might complicate the description). Furthermore, Zhang *et al.* [60] showed that when quantum effects are included in the calculations, the reorientation appears to be the rate limiting step below 600 K. Raiteri *et al.* [61] found an activation energy for transfer almost an order of magnitude lower than that of rotation. In this study, the authors also underline that the activation energy values are dependent on the functional used, the lattice parameters, and on the dimension of the supercell.

Whereas on one hand computational studies have to face discrepancies in

results depending on the chosen computational details, on the other hand experimentalists have to consider the effect on reproducibility introduced by samples prepared with different synthesis routes. To illustrate this, Groß, Beck and collaborators investigated the influence of grain size in hydrated Y-doped barium zirconates using QENS [62, 63]. The microcrystalline material, prepared by solid-state synthesis, showed a signal related to a strongly localized hydrogen motion, whereas for the nanosized material, obtained by sol-gel synthesis, it was hypothesised the presence of a non-structured hydrogen motion in the grain boundary regions or on the surface of the crystallites. Even apparently smaller differences in the preparation of the samples may lead to sensibly different results: the study of Azad *et al.* [64] presents two cubic polymorphs of Y-doped barium zirconates showing different conductivity values, obtained by changing the annealing conditions. Moreover, the possible impact of the hydration degree and of the presence of different additional hydrogenated species which may form during the various steps of the synthesis and hydration of the samples is also debated and under investigation [26, 65, 66].

Within the experimental studies, a crucial contribution to the understanding of the proton conduction mechanism arose from QENS investigations [67]. As it will be detailed in the next chapters, depending on the instrumental details of such experiments it is possible to gain information regarding the single steps (localized dynamics) of the Grotthuss mechanism or on the resulting overall long-range proton diffusion. However, the choice of such details and the subsequent interpretation of the observed processes might be indeed not trivial. Dynamics with localized character were identified for perovskites having the following nominal compositions: $Ba_3Ca_{1.18}Nb_{1.822}H_{0.2}O_{8.83}$ [68], $SrCe_{0.95}Yb_{0.05}H_{0.02}O_{2.985}$ [69], $Ba_3Ca_{1.18}Nb_{1.822}H_{0.2}O_{8.83}$ [53], $BaZr_{0.9}Y_{0.1}H_{0.1}O_3$ [70, 71], $BaZr_{0.85}Y_{0.15}H_{0.15}O_3$ [62, 63], $BaZr_{0.9}Sc_{0.1}H_{0.1}O_3$ [70], and $BaZr_{1-x}Ln_xH_xO_3$ (x=0.06 and 0.03) [72]. The observed dynamics was generally found to be thermally activated with an

onset temperature of around 260–300 K and associated activation energies ranging from few tens of meV to *ca* 100 meV. Such motions have been mainly interpreted as the reorientational step, although localized transfers are in some cases consistent. For example, on the basis of the comparison with computational data, a higher compatibility of the observed motion with intra-octahedral proton transfer was conjectured for acceptor doped barium zirconates [70]. In the same study, the authors attempted to distinguish between transfer and reorientation on the basis of the geometry of the observed dynamics. However, the limited length scale accessible within the experiment did not allow such a discrimination [70]. The geometry of the motion was investigated also in the study of Matzke *et al.* [69], turning out to be compatible with several tested hypotheses. QENS also allowed for the identification of proton diffusion in samples with nominal compositions of $SrCe_{0.95}Yb_{0.05}H_{0.02}O_{2.985}$ [69, 73], $Ba_3Ca_{1.18}Nb_{1.822}H_{0.2}O_{8.83}$ [53, 68], $SrZr_{0.95}Y_{0.05}O_3$ [74], $BaZr_{0.9}Y_{0.1}H_{0.1}O_3$ [75, 76], and $BaCe_{0.8}Y_{0.2}H_{0.2}O_3$ [77, 78]. Compared with the localized motions, activation energies are generally higher, roughly in the range 0.15–0.45 eV. For $BaCe_{0.8}Y_{0.2}H_{0.2}O_3$ and $BaZr_{0.9}Y_{0.1}H_{0.1}O_3$, Braun *et al.* [75, 77] conjectured a change in proton relaxation towards dynamics governed by lower activation energies at temperatures below *ca* 700 K. In the cases for which the experimental parameters allowed for a more detailed analysis of the mechanism, jump diffusion models such as the Chudley-Elliot model [79] are usually proposed, in accordance to the proton hopping outlined by the Grotthuss mechanism. However, the derived jump lengths in the different studies found rough correspondance with different distances in the structures: for example O-O distances in the studies of Hempelmann and coworkers [69, 73], short interoctahedral jumps in that of Sata *et al.* [74], and next nearest O-O neighbours in those of Braun and coworkers [75, 77, 78]. The last group, in their recent study on Y-doped cerates [78], also proposed an analysis that couples proton and lattice dynamics in accordance with the proton-

polaron model previously introduced by Samgin [80]. Several studies showed that the host lattice is not a mere spectator in the proton conduction mechanism but plays a crucial role, facilitating proton diffusion by its vibrational dynamics [12, 13, 26, 57, 60, 77, 78, 81–83]. However, how exactly this phonon assistance should be taken into account in modelling the proton conduction mechanism is not yet unambiguously determined [12, 13].

As seen, albeit some agreement for a Grotthuss mechanism is nowadays reached, as well as for an involvement of the lattice dynamics, additional studies are still required in order to understand in detail proton dynamics at the atomic length scale, thus providing pivotal knowledge for the design of new proton conducting materials. The influence of the acceptor doping deserves particular attention due to the strong impact on the observed proton conductivity, thus likely constituting central information for the development of improved proton conductors.

Influence of the acceptor doping on proton dynamics

The acceptor dopant (and analougously the mixed occupancy on the B-site) induces local structural and chemical perturbations towards which proton mobility is sensitive [3, 84–87]. For example, local distortions induced by the dopant (M) are reported for barium zirconates with M= In [54, 84, 88, 89] and M= Y [90], or in Y-doped barium cerates [91]. How specifically these perturbations influence the proton conduction mechanism has not been completely disentangled.

The most commonly shared view is that the dopant acts as a relatively localized trapping centre for the protons, changing the character of the coordinated oxygens and making the protons spend longer times in their vicinity before being able to further diffuse. The first author to introduce this idea was Hempelmann in 1995, on the basis of QENS data for proton diffusion in $SrCe_{0.95}Yb_{0.05}H_{0.02}O_{2.985}$ [69, 73, 92]. With his collaborators, he identified two

components in the observed dynamics, which were interpreted as the consequence of two different sites occupied by the protons, in a trapping and release scenario. In this picture, the protons quite freely move in dopant-free regions of the perovskite matrix with a characteristic transition rate, giving rise in the experiment to the component corresponding to the fastest dynamics, and are trapped by the dopant cations on some longer time scale, appearing in the experiment as the slowest component. In the subsequent years, the same group supported this view with a similar investigation on BCN18 [68], although the slow dynamics corresponding to the trapped state could not be resolved in that study, and with a muon spin relaxation study on Sc-doped strontium zirconate [93]. More recently, Yamazaki *et al.* [94] presented a study with nuclear magnetic resonance combined with conductivity measurements on barium zirconates doped with 20% of Y [94]. The authors proposed a picture in which the protons are largely trapped in the vicinity of the dopant, where they can undergo local motions such as transfers and reorientation with an activation energy of 13–16 kJ/mol. To leave the trap sites they need to overcome an activation energy of 29 kJ/mol, being subsequently able to long-range migrate in the trap-free region. For the diffusion in the trap-free region, an activation energy of 13–16 kJ/mol, *i.e.* similar to that in the vicinity of the dopant, was advanced. A trapping behaviour of the dopant was also supported by several simulation studies which found a reduction of the proton mobility and increased activation energies in the vicinity of the dopant sites [57, 61, 81, 95–98], and by a luminscence spectroscopy study [99], where attractive interaction between protons and dopant atoms were observed.

In a different hypothesis, the dopant acts in a less structurally localized fashion. This was proposed on the basis of conductivity measurements on Y-doped barium cerates, which showed a decreasing proton mobility with increasing doping level, as a result of a generally increased activation energy [56]. Although

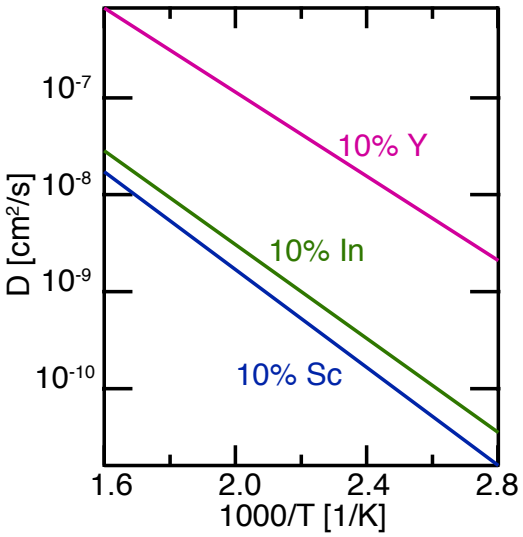

Figure 2.6: Proton diffusion coefficents obtained from conductivity measurements for 10% Y-, Sc- and In-doped barium zirconates. Values are taken from Ref. [86].

this view has encountered less support by following studies, recent QENS data showing diffusion characterized by a unique activation energy were interpreted within this homogeneous relaxation scenario [75, 77, 78].

Under either role of the dopant, the doping type in terms of chosen ion and concentration has clearly a strong influence on the proton conduction. Looking for example at the proton diffusion coefficents obtained from conductivity measurements reported for cubic barium zirconates by Kreuer *et al.* [86], Figure 2.6, it is possible to note that different dopant atoms may lead to very different proton mobilities, in spite of the similar averaged structure of the materials. At 500 °C, 10%-Y-doped barium zirconate shows a diffusion coefficient of the order of 10^{-6} cm^2/s, *i.e.* one order of magnitude higher than the Sc- or In-doped counterparts. The same experimental trend found for proton mobility was reproduced by a density functional theory study [57]. Several properties of the dopant ions have been considered to play a significant role in determining these differences: the ionic radius [57, 86, 100], the different types of oxygen-

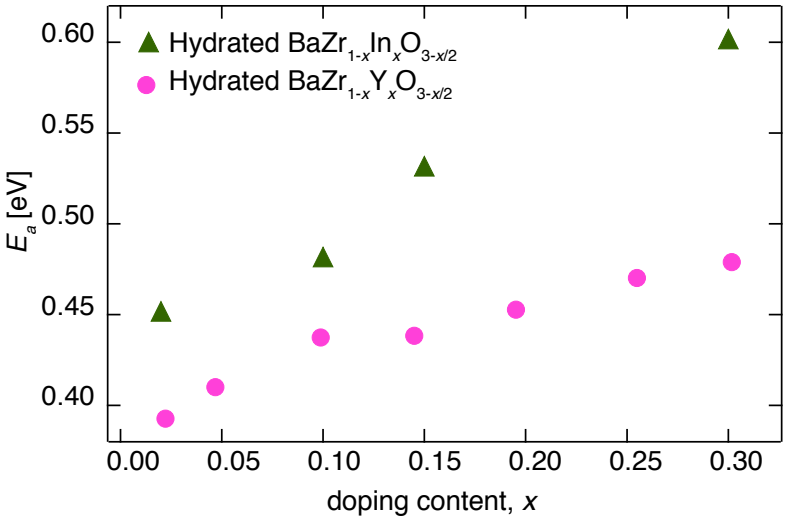

Figure 2.7: Activation energies obtained from impedance spectroscopy on a series of Y-doped barium zirconates (bulk conductivity) and In-doped barium zirconates (unspecified). Values are taken from Ref. [103] and [88], respectively.

dopant bonding depending on the electronic structure [86, 100, 101], and the absolute hardness [102]. Proton dynamics in 10%-doped barium zirconates with Y and Sc as a dopant was investigated with QENS [70]. Results showed similar activation energy and relaxation time for the localized dynamics of the two materials. Regarding the effect on the conductivity of the doping level, conductivity measurements on a series of Y-doped barium zirconates [103] and impedance spectroscopy on a series of In-doped barium zirconates [88] revealed increased activation energy as a function of the doping content (Figure 2.7). In-doped barium zirconates with a doping level of 10% and 50% were investigated with QENS [104], suggesting a complex dynamics for the highly doped material, whereas for the 10% doped material the relaxation was interpreted as a unique process.

2.2 Aims of the study and investigated systems

Given the background and ideas developed above, the aim of the studies presented in this thesis was to provide more details on the proton conduction mechanism in proton conducting oxides, both regarding localized dynamics and non-localized diffusion. In particular, the focus was onto two central questions:

- What is the effect of **different dopant ions** on the proton conduction mechanism?

- What is the effect of **different doping concentration** on the proton conduction mechanism?

To shed more light on these points, acceptor doped barium zirconates were chosen because of their great promise. Specifically, the selected samples were hydrated $BaZr_{0.9}M_{0.1}O_{2.95}$ (M = Y, Sc and In) and hydrated $BaZr_{1-x}In_xO_{3-x/2}$ (x = 0–0.275), as summarised in Figure 2.8. To investigate the effect of the dopant atom (Papers I-II and V), the doping level was kept low (10%), in order to preserve the cubic symmetry [86]. The oxide ion sites are therefore equivalent, making possible effects introduced by the dopant atoms clearer. Also local distorsions, albeit present, are shown to be small for this relatively low doping level [89]. The dopants were also chosen to match the extreme values in proton conductivity, as reported elsewhere [86]. Within the group of proton conducting barium zirconates, the yttrium-doped material shows the highest conductivity, whereas the scandium-doped material shows one of the worst [86]. For similar reasons, to study the effect of the doping level (Papers III–V), In was chosen as dopant atom. Indeed, it has been shown that this dopant preserves the average cubic symmetry even at high concentration [105], as opposed to Y [3], for example, although local distorsions are present [54, 85, 88]. Moreover, it is easy to incorporate In as dopant in the barium zirconate structure at various

concentrations, making possible to further extend the series in future studies, and it is possible to achieve high hydration degrees, thus providing a good contrast in the experiments [88, 102], as it will be detailed in the next chapters.

To conduct such investigations, neutron scattering techniques, and notably neutron spectroscopy in the quasielastic region have been used. In the next chapters, a short introduction to neutron scattering, focusing on the essentials needed to understand the work presented in the five appended papers, will be given.

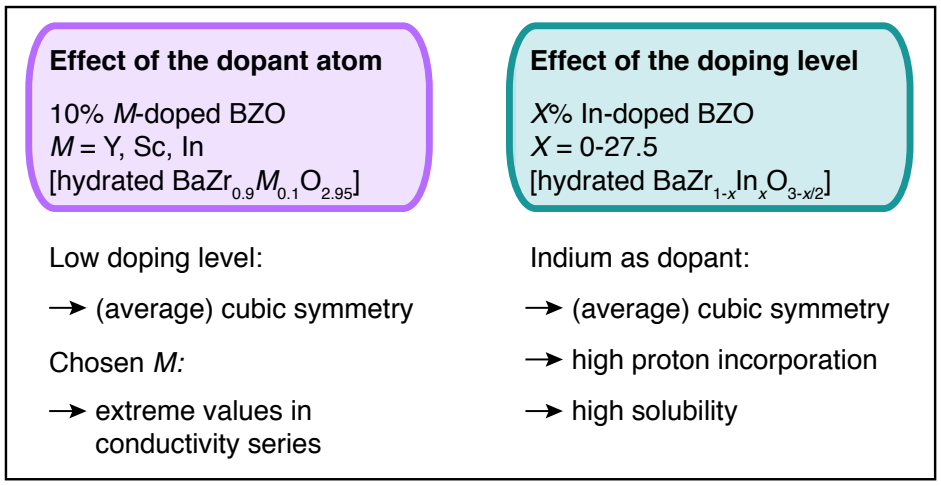

Figure 2.8: Overview of the materials investigated in this study.

Chapter 3

Basics of neutron scattering

Neutron scattering is an extremely powerful and versatile experimental method for materials science. A comprehensive treatment of neutron scattering is beyond the aim of this thesis, and thus this chapter rather presents the basic concepts allowing the reader to follow the interpretation of the measurements here reported. After a short introduction on the general formalism to describe the outcome of a neutron scattering experiment, the focus is set mainly onto the features of QENS. The quasielastic regime is where diffusing or reorientating particles leave the signature of their dynamics. For this reason, it was the main technique of the investigations in this project. A short section about the advantages of the use of polarized neutrons will be also given. A more extensive treatment of neutron scattering can be found in Ref. [106–108], which are the main references in this chapter, if not otherwise indicated. The needed notions of quantum mechanics can be found, for example, in Ref. [109].

3.1 Theoretical introduction and basic definitions

Neutrons can be produced and moderated to have wavelengths comparable with interatomic distances, having consequently energies of the same order of that of many excitations in condensed matter. At these conditions ("slow neutrons", *i.e.* having energies from meV to tenths of an eV and wavelengths from 10 Å or more to tenths of an angstrom [110]) the interaction between neutrons and matter is weak, thus the physical and chemical properties of the samples are not perturbed by the probe. Moreover, being electrically uncharged they can easily penetrate most materials. Neutrons are therefore a unique probe for the investigation of both atomic structure and dynamics in condensed matter.

Neutrons interact with the atoms of the sample directly with the nuclei (*via* the strong nuclear force) and with the magnetic moment of the unpaired electrons (*via* the magnetic moment of the neutron). Since the case of magnetic scattering is not relevant for the here investigated materials, it will not be treated in the discussion hereafter. The nuclear interaction has a very short range, orders of magnitude smaller than the wavelength of the neutron. As a consequence, the leading term in the neutron-nucleus interaction is of s-wave character, and higher order terms are negligible. It can be therefore characterized by a single parameter, b, called the scattering length. This quantity varies randomly with the atomic number, and also depends on the mass number and the spin state of the neutron-nucleus system.

In a neutron scattering experiment, the incoming neutron is represented by a plane wave characterized by a wave vector $\mathbf{k}_\mathrm{i}$. Its magnitude k_i defines the

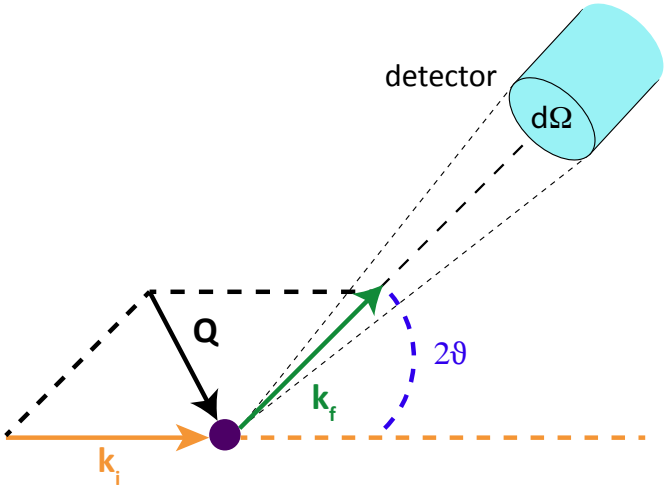

Figure 3.1: Schematic representation of the scattering experiment, and relations among the initial and final wavevectors, $\mathbf{k}_\mathrm{i}$ and $\mathbf{k}_\mathrm{f}$, and the scattering vector $\mathbf{Q}$. 2ϑ is the scattering angle, and $d\Omega$ is the collection solid angle of the detector.

initial wavelength $\lambda_\mathrm{i} = 2\pi k_\mathrm{i}^{-1}$. The energy of the incident neutron is

$$E_i = \frac{\hbar^2 k_\mathrm{i}^2}{2m_\mathrm{n}}, \tag{3.1}$$

where m_n is the neutron mass and $\hbar$ is the reduced Planck constant. Figure 3.1 shows the relationship among the initial wavevector $\mathbf{k}_\mathrm{i}$, the final wavevector $\mathbf{k}_\mathrm{f}$ and the scattering vector Q, defined as

$$\mathbf{Q} = \mathbf{k}_\mathrm{i} - \mathbf{k}_\mathrm{f}. \tag{3.2}$$

The conservation of momentum and energy implies that the momentum transfer from the neutron to the sample is $\hbar\mathbf{Q}$ and the energy transfer is

$$\Delta E = E_\mathrm{i} - E_\mathrm{f}, \tag{3.3}$$

where the final energy E_f can be derived from the magnitude of the final vector k_f in analogy to Eq. 3.1. In this definition of the energy transfer, a positive value

of ΔE corresponds to neutron energy loss. The magnitude of the scattering vector can be expressed as

$$Q^2 = k_f^2 + k_{\mathrm{i}}^2 - 2k_{\mathrm{i}}k_{\mathrm{f}}\mathrm{cos}2\vartheta \;\; = \\ \frac{2m_{\mathrm{n}}}{\hbar^2}\left(2E_{\mathrm{i}} - \Delta E - 2\sqrt{E_{\mathrm{i}}\left(E_{\mathrm{i}} - \Delta E\right)}\mathrm{cos}2\vartheta\right), \tag{3.4}$$

where 2ϑ is the scattering angle between the incident and scattered wavevectors. For elastic scattering ($\Delta E = 0$), or for scattering processes where $|\Delta E| \ll E_{\mathrm{i}}$, the magnitude of the scattering vector can be simplified to

$$Q_{el} = \frac{4\pi}{\lambda_{\mathrm{i}}}\mathrm{sin}\vartheta. \tag{3.5}$$

From Eq. 3.4, it is clear that the region of the energy-momentum transfer space which can be explored in a neutron scattering experiment is limited and depends on both the initial energy of the neutrons and the minimum and maximum scattering angle that can be probed during the experiment. Figure 3.2 shows a representation for an initial wavelength of 3 Å.

As for the the measured intensity of the scattered neutron beam, this is proportional to the double differential cross section, which gives the fraction of neutrons of incident energy E_i scattered within the space defined by the differential solid angle $d\Omega$ and having a final energy in the interval $[E_{\mathrm{f}}, E_{\mathrm{f}} + dE_{\mathrm{f}}]$. Within the Born approximation, it takes the form:

$$\frac{\mathrm{d}^2\sigma}{\mathrm{d}\Omega\mathrm{d}\mathrm{E}_{\mathrm{f}}} = \frac{k_{\mathrm{f}}}{k_{\mathrm{i}}2\pi\hbar}\sum_{ij}^{N}\overline{b_i^* b_j}\int\left\langle e^{-i\mathbf{Q}\cdot\mathbf{r}_i(0)}e^{i\mathbf{Q}\cdot\mathbf{r}_j(t)}\right\rangle e^{-i\omega t}\mathrm{d}t, \tag{3.6}$$

where the angular brackets denote a thermal average, the horizontal bar represents an average over nuclear spin orientation and distributions, and $\mathbf{r}_i(t)$ is the position of the scatterer i at time t. Considering a monoatomic target, the

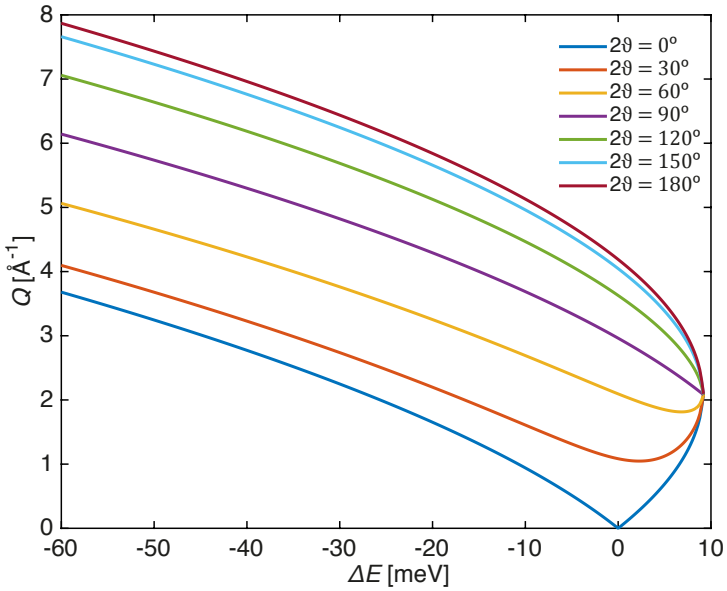

Figure 3.2: Accessible dynamic range for a neutron beam with λ_i= 3 Å. The lines represent the energy transfer associated with a given Q under specific scattering angles 2ϑ. The regions outside the lines for 0 and 180°cannot be accessed with neutrons.

summation in Eq. 3.6 can be split into a part concerning the time correlations between N different scatterers ($i \neq j$) and one for self correlations ($i = j$), yielding the following relation:

$$\frac{\mathrm{d}^2\sigma}{\mathrm{d}\Omega \mathrm{dE_f}} = \frac{k_\mathrm{f}}{k_\mathrm{i} 2\pi\hbar}\left[\sum_{i\neq j}^{N} \overline{b}^2 \int \left\langle e^{-i\mathbf{Q}\cdot\mathbf{r}_i(0)} e^{i\mathbf{Q}\cdot\mathbf{r}_j(t)}\right\rangle e^{-i\omega t}\mathrm{dt} \quad + \right.$$
$$\left. \sum_{i}^{N} \overline{b^2} \int \left\langle e^{-i\mathbf{Q}\cdot\mathbf{r}_i(0)} e^{i\mathbf{Q}\cdot\mathbf{r}_i(t)}\right\rangle e^{-i\omega t}\mathrm{dt}\right]. \tag{3.7}$$

The coherent and incoherent dynamic structure factors are introduced, as

$$S_\mathrm{coh}(\mathbf{Q},\omega) = \frac{1}{2N\pi\hbar}\sum_{ij}^{N} \int \left\langle e^{-i\mathbf{Q}\cdot\mathbf{r}_i(0)} e^{i\mathbf{Q}\cdot\mathbf{r}_j(t)}\right\rangle e^{-i\omega t}\mathrm{dt} \tag{3.8}$$

and

$$S_{\mathrm{inc}}(\mathbf{Q},\omega) = \frac{1}{2N\pi\hbar}\sum_{i}^{N}\int \left\langle e^{-i\mathbf{Q}\cdot\mathbf{r}_i(0)}e^{i\mathbf{Q}\cdot\mathbf{r}_i(t)}\right\rangle e^{-i\omega t}\mathrm{dt}, \tag{3.9}$$

respectively, together with the coherent and incoherent scattering cross sections:

$$\sigma_{\mathrm{coh}} = 4\pi\bar{b}^2 \tag{3.10}$$

and

$$\sigma_{\mathrm{inc}} = 4\pi\left(\overline{b^2} - \bar{b}^2\right). \tag{3.11}$$

It follows that Eq. 3.7 can be rewritten as

$$\frac{d^2\sigma}{d\Omega dE_{\mathrm{f}}} = \frac{Nk_{\mathrm{f}}}{4\pi k_{\mathrm{i}}}\left[\sigma_{\mathrm{coh}}S_{\mathrm{coh}}(\mathbf{Q},\omega) + \sigma_{\mathrm{inc}}S_{\mathrm{inc}}(\mathbf{Q},\omega)\right] \tag{3.12}$$

The coherent scattering depends on the correlation between the positions of the same nucleus at different times (self correlation [111]) and on the correlation between the positions of different nuclei at different times (distinct correlation [111]). It thus comprises interference effects. It is proportional to the squared average of the scattering length. Its intensity presents a strong anisotropy. For example, considering elastic scattering in crystals, intensity peaks appear for the particular directions of the scattered beam that satisfy the Bragg condition, $\lambda = 2d\sin\vartheta$, where λ is the wavelength, d is the lattice parameter and 2ϑ is the angle between the incoming and reflected beam. The incoherent scattering depends on the correlation between the positions of the same nucleus at different times (self correlation [111]), and it is proportional to the standard deviation of scattering lengths in the system.

The time Fourier transforms (FTs) of the coherent and incoherent dynamic structure factor give the coherent and incoherent intermediate scattering function $I_{\mathrm{coh}}(\mathbf{Q},t)$ and $I_{\mathrm{inc}}(\mathbf{Q},t)$, respectively [111]. These functions are the space

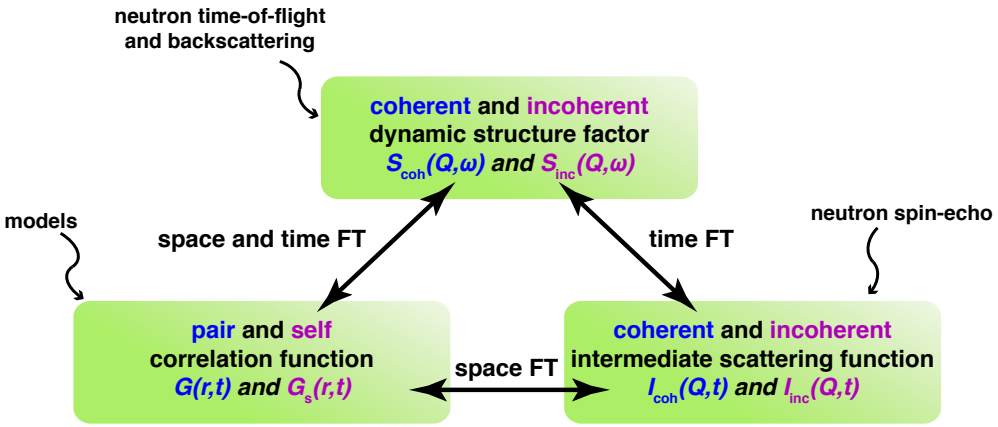

Figure 3.3: Relationship between different functions used in neutron scattering. The functions are related to each other by time and/or space Fourier transformations (FTs).

FTs of the pair and self correlation functions $G(\mathbf{r},t)$ and $G_s(\mathbf{r},t)$, respectively. The pair correlation function describes the probability of finding any particle at distance $\mathbf{r}$ and after a time t in relation to the position of a given particle at $t = 0$. The self correlation function gives the probability of finding exactly the same particle at distance $\mathbf{r}$ and after time t. A diagram describing the relationships within these different functions and their accessibility by different methods is given in Figure 3.3.

Finally, it is possible to note that the particularly large incoherent scattering cross section of hydrogen makes neutron scattering notably suitable for the study of proton self-diffusion, enabling the investigation even in materials with relatively low amounts of protons, such as the proton conductors investigated in this thesis. Table 3.1 summarises the cross sections for the different atoms in the investigated materials.

Element	σ_{scatt} [barn]	σ_{coh} [barn]	σ_{inc} [barn]	σ_{abs} [barn]
H	82.03	1.7568	80.27	0.3327
O	4.233	4.233	0.0008	0.00019
Sc	23.6	19.0	4.5	27.5
Y	7.71	7.55	0.16	1.28
Zr	6.46	6.44	0.02	0.185
In	2.62	2.08	0.54	193.8
Ba	3.38	3.23	0.15	1.1

Table 3.1: Scattering (coherent and incoherent) and absorption cross sections for the elements composing the materials investigated in this study. 1 barn = 10^{-28} m^2. σ_{scatt} is the total scattering cross section. Absorption cross sections are reported for $\lambda_i = 1.798$ Å. Values are taken from Ref. [112].

3.2 Quasielastic neutron scattering

As seen, neutrons are an effective probe to investigate both structure and dynamics in materials. Inelastic processes ($\Delta E \neq 0$) are those that allow to gain information on dynamics, which lies at the heart of this thesis. QENS is a type of inelastic neutron scattering (INS) in which the exchanged energy between the sample and the neutrons is small, *i.e.* is almost (*quasi*) elastic. It is typically associated with relaxation phenomena, such as translational diffusion, molecular reorientations etc. It is centred at the elastic line ($\Delta E = 0$), and it is manifested as a broadening of the elastic line by a continuous distribution of energies, characterized by its half width at half maximum. Typical energies of QENS are in the orders of meV or μeV, corresponding to a time window of roughly 10^{-10}–10^{-12} s. Faster motions, out of the quasielastic window, give rise to features at higher exchanged energies, *i.e.* the inelastic components, typically associated with lattice or localized excitations. A sketch of the elastic, inelastic and quasielastic scattering components in a spectrum is given in Figure 3.4.

An accurate investigation of the shape of the quasielastic component and of

the dependency of the broadening (or analogously of the time decay[1]) on the momentum transfer yield information on the physical nature of the motions of the scatterers [113, 114]. Further, in the case of localized or confined motion, the analysis of the Q-dependence of the relative amplitudes of the elastic and quasielastic components gives insights into the spatial geometry of the dynamics [113, 114] (*cfr* Papers II-III, and V).

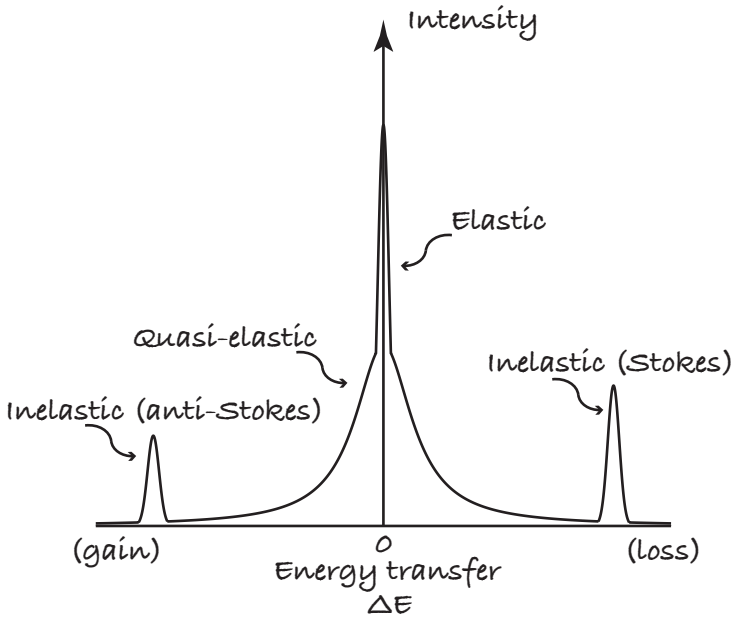

Figure 3.4: Sketch of the elastic, quasielastic and inelastic components in a neutron scattering spectrum. According to the definitions given in section 3.1, *gain* and *loss* refer to neutron energy gain and neutron energy loss, respectively.

[1]As seen, the $Q-\omega$ and the $Q-t$ phase-spaces are related trough FT. It follows that a broadening registered in the $Q-\omega$ phase-space is equivalent to a decay in the $Q-t$ phase-space.

3.3 Polarization analysis and separation of coherent and incoherent components

Equation 3.7 shows that the measured signal in a scattering experiment has two contributions: coherent and incoherent. For their separation, the neutron spin can be exploited, by means of polarized neutrons, *i.e.* neutrons all having the same spin orientation [115–118].

The statistical distribution of nuclear scattering lengths can have its origin in the atomic isotopes or in the nuclear spin state. This implies two contributions for the incoherent scattering: spin-incoherent and isotope-incoherent [112]. Coherent scattering and isotope incoherent scattering do not change the spin state of the neutron, *i.e.* they are non-spin-flip processes [115, 116]. Spin-incoherent scattering, conversely, has a probability of 2/3 to change the spin state of the neutron. Polarized neutrons can be therefore used to separate the different scattering contributions [115–118]. The spin-flip and non-spin-flip cross sections are measured for three orthogonal orientations of the neutron beam polarization. From linear combinations of these, the nuclear, spin incoherent, and magnetic contributions are extracted [115–118]. Further details of this technique, called xyz-polarization analysis, can be found in Ref. [117, 118].

Chapter 4

Experimental details

Having briefly reviewed the theoretical aspects of neutron scattering of main importance for this thesis, here the focus is moved onto its technical part. Different neutron techniques give access to different time and length scales, therefore providing information that are complementary to each other. Figure 4.1 gives a glance over the different ranges covered by neutron scattering methods, highlighted as polygons in bright colours and shown together with other complementary experimental techniques, and on the many different materials and systems that can be studied.

Neutron time-of-flight (ToF), backscattering (NBS) and spin-echo spectroscopy (NSE) are the main experimental techniques used in this study. All these experimental techniques have their strengths and limitations, thus combining them in a systematic study is crucial to gain new insights into the proton conduction mechanism.

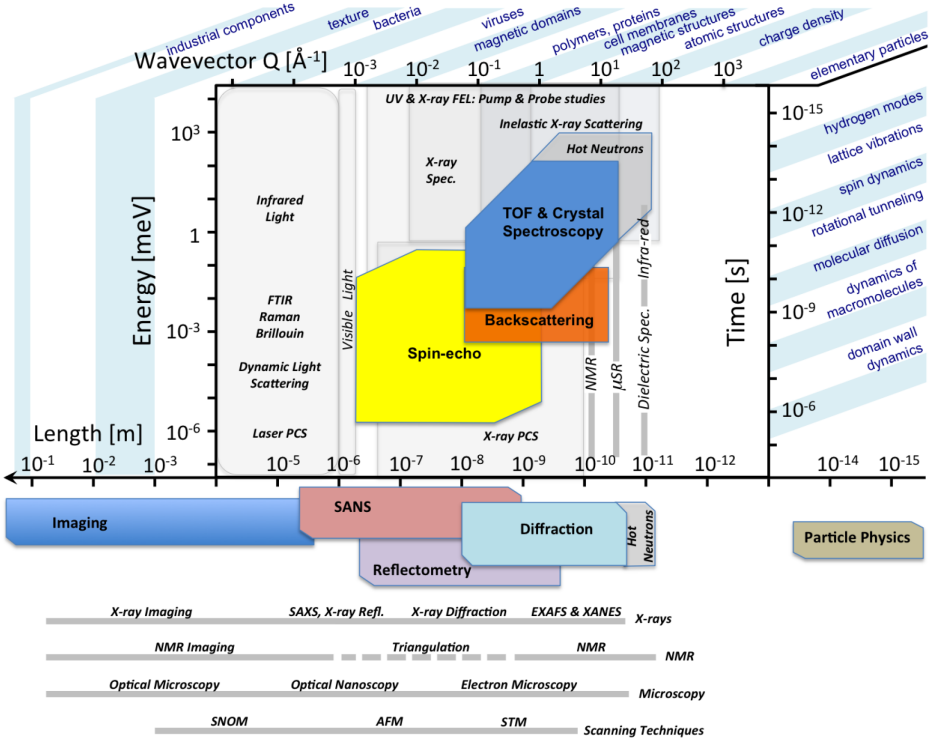

Figure 4.1: Phase-space coverage of different neutron scattering techniques. The various neutron scattering methods provide information about the properties and behaviour of many different materials and systems. The horizontal axes indicate real and reciprocal length scales, whereas the vertical axes refer to time and energy scales. Along the edges, scientific areas falling within different length and time scales are indicated. The experimentally accessible areas of the various neutron-based techniques are shown as polygons in bright colours. A selection of complementary experimental techniques is shown in grey. Figure courtesy of Arno Hiess [119].

4.1 Neutron time-of-flight spectroscopy

In the ToF method, the neutron is considered as a classical particle, and its energy is determined by measuring the time that it needs to cover a known distance. If a neutron with mass m_{n} travels over a distance L in a time Δt, it is possible to express its kinetic energy as

$$E = \frac{1}{2} m_{\mathrm{n}} v^2 = \frac{h^2}{2 m_{\mathrm{n}} \lambda^2} = \frac{m_{\mathrm{n}} L^2}{2 \Delta t^2}, \tag{4.1}$$

where λ and v are the wavelength and velocity of the neutron, respectively, and h is the Planck constant. If during the scattering event the neutron wavelength changes, due to inelastic scattering, this corresponds to a change of the velocity and therefore of the time-of-flight of the scattered neutron [113, 120].

The instruments that apply the ToF method to determine the energy transfer, after having selected an initial energy, are usually called direct geometry ToF spectrometers. In this type of instruments, the incident neutron beam needs to be pulsed and monochromatized. The monochromatization defines a precise wavelength of the neutron before the scattering event. However, neutrons in a continuous monochromatic incident beam would be indistinguishable. Pulsing the beam permits to label them: all the neutrons travelling in a monochromatic pulse have the same, well-defined, initial time. Conversely, they differ in their arrival time to the detector banks, depending on whether they have lost, gained or conserved their initial energy during the scattering with the sample. Some instruments make use of the ToF method to achieve a pulsed monochromatized incident beam, with a series of disk choppers: absorbing disks with transparent slits, turning in the plane perpendicular to the beam direction. This is the case of the IN5 spectrometer at the Institut Laue-Langevin (ILL) in Grenoble (France), whose scheme is depicted in Figure 4.2 and that was used for the measurements

of Paper II. The beam is first pulsed by the two counter-rotating disks forming the pulsing chopper system (P). The contaminant chopper (CO) reduces the large bandwidth by removing higher order harmonics, and the frame overlap chopper (FO) suppresses some of the produced pulses, in order to avoid that the slowest neutrons from a pulse mix at the detector with the fastest neutrons from the next pulse. The monochromator choppers (M) are two counter-rotating disks that, being synchronized with the pulsing chopper, allow the passage of neutrons with only a desired wavelength, absorbing all the neutrons which travel faster or slower. The direct ToF instruments using this technology are usually called disk chopper direct geometry ToF, or also ToF-ToF spectrometers, since they use the ToF method twice: to pulse and monochromatize the incident beam and also to record the energy transfer. TOFTOF at the Forschungs-Neutronenquelle Heinz Maier-Leibnitz (FRM II) in Garching (Germany), used for the measurements reported in Paper IV, is another example of this kind of instruments and is very similar to IN5. One of the main differences, from the point of view of the users, is the detector. Both instruments use detectors based on ^{3}He technology: TOFTOF has 1000 tubes covering about 12 m^2, whereas IN5 has 384 position sensitive tubes (PSD), covering about 30 m^2. The use of PSD tubes allows a determination of the position of the point of impact, and therefore of $\mathbf{Q}$; thus IN5 can be exploited also for single crystals measurements. In other direct geometry ToF instruments, like IN6 at ILL, the incoming wavelength is selected by a single-crystal monochromator, and the beam is then pulsed by a Fermi chopper, *i.e.* a collimator turning around an axis perpendicular to the beam direction. These instruments are sometimes called direct geometry hybride ToF.

The energy resolution in the ToF instruments is determined by the wavelength dispersion of the incoming neutron pulse, which depends on the dimension of the opening and the rotating speed of the chopper, and by the uncertainty related to the flight path, which includes the beam divergence, the thickness of

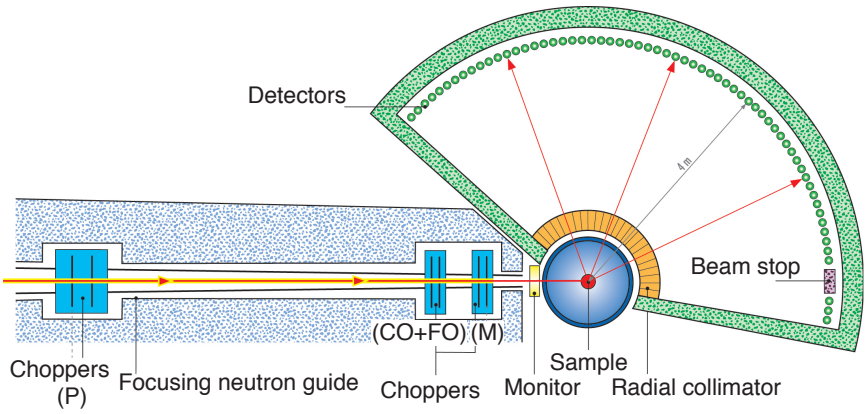

Figure 4.2: Schematic representation of the IN5 tof spectrometer at ILL. Figure courtesy of the ILL.

the sample, and the detector size. Increasing the resolution is therefore paid with a loss of intensity [120–122]. To achieve high resolution, long wavelengths are required, with consequent strong limitations to the achievable Q-E range.

On the other hand, one of the main strengths of the ToF spectrometers is their great flexibility in choosing the energy resolution (from μeV to meV) and the energy and momentum transfer range, adapting to many different experimental needs [120–122].

Of relevance here, QENS at ToF instruments can provide information on the fundamental steps of the proton diffusion in proton conductors, *i.e.* proton transfers between neighbouring oxygens and reorientations of the -OH group. More specifically, the wide Q-range offered by this kind of spectrometers can be exploited to conduct investigations regarding the geometry of these dynamics, by analysing the Q dependence of the relative intensity of the elastic and quasielastic contributions. Paper II and III deal with this aspect, exploiting measurements done at the direct geometry disk choppers spectrometers IN5 at the ILL and TOFTOF at FRM II. Moreover, the wide dynamical range of these instruments can be used to simultaneously explore the inelastic spectrum, which is related to vibrational dynamics. In Paper II this feature was used to

derive the proton vibrational mean-square displacements, and in Paper III the generalised density of states was determined.

4.2 Neutron backscattering spectroscopy

In a NBS spectrometer, the energy analysis of the scattered neutrons and the monochromatization of the incoming neutron beam are achieved by single crystals used in backscattering geometry, *i.e.* with scattering angle $2\vartheta \approx 180°$ [120, 121, 123]. The backscattering geometry is crucial to achieve high energy resolution, which is improved by one or two orders of magnitude in respect to the ToF instruments, therefore allowing to study processes at a time scale up to some nanoseconds, while maintaining a considerable Q-range, usually around 0.2–2 Å^{-1}. The importance of the backscattering condition to achieve a high resolution appears clear differentiating the Bragg-condition. The result is

$$\frac{\Delta\lambda}{\lambda} = \frac{\Delta d}{d} + \Delta\vartheta \cot\vartheta, \tag{4.2}$$

and it can be therefore noticed that the reflected wavelength uncertainty $\Delta\lambda$ becomes minimal for $\vartheta = 90°$. Moreover, in the backscattering condition, the width of the reflected wavelength uncertainty is independent, in this first order approximation, from the beam divergence $\Delta\vartheta$ and only depends on the term $\Delta d/d$, which is related to the quality of the crystal [123].

Figure 4.3 shows a scheme of the NBS spectrometer IN16b [124] at the ILL, used for the measurements reported in Paper V, illustrated in its "high flux" configuration. The incident wavelength band is selected by a velocity selector. The background chopper pulses the beam, and a rotating deflector sends the beam to the monochromator, where the energy is selected with high precision. Due to the pulsed structure of the beam, the neutrons reflected by the monochromator

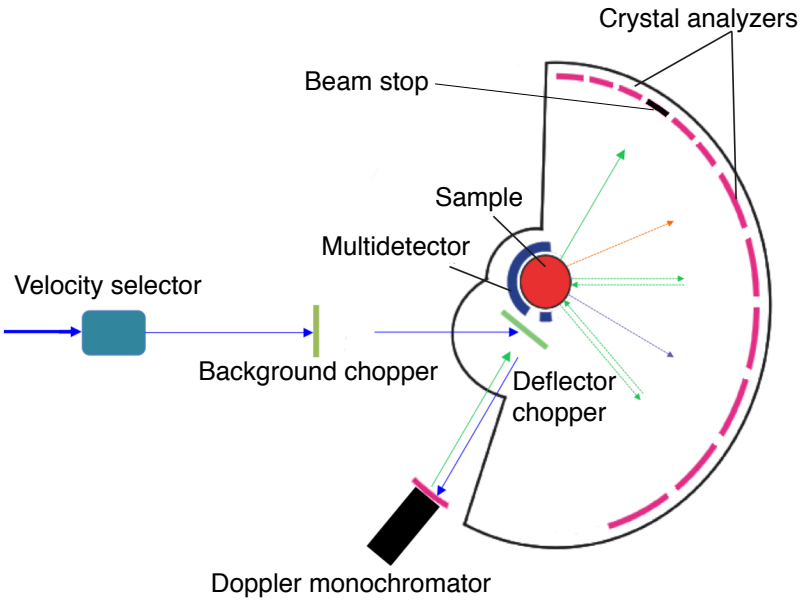

Figure 4.3: Schematic representation of the IN16b NBS spectrometer at ILL, redrawn from Ref. [125].

are allowed to pass back through an open window in the rotating deflector and reach the sample, by which they are scattered in all directions. Only those neutrons having a certain final energy, determined by the backscattering reflection at the analyser crystals, are reflected to the detectors and counted.

The monochromator is mounted on a Doppler device that allows to move it backwards and forwards with different velocities. The energy of the neutrons after reflection from a moving monochromator is $E_i + \Delta E$, where E_i is the neutron energy that would be reflected by the monochromator at rest, and ΔE is

$$\Delta E = 2\frac{v_D}{v}E_i, \tag{4.3}$$

where v is the neutron velocity and v_D the Doppler velocity. This is valid in a first order approximation for $v_D \ll v$ [123].

Depending on the working conditions of the Doppler, different types of mea-

surements can be done:

- Elastic fixed window scan (EFWS): the monochromator is resting, and all the neutrons reaching the detector have therefore been scattered elastically (within the instrumental resolution) by the sample. Recording the elastic intensity as a function of sample temperature allows to draw conclusions upon the microscopic dynamics of the compound. For example, for a compound displaying harmonic dynamics due to phonon modes, the elastic intensity is modulated by the Debye-Waller factor $DWF = \exp\left(\frac{-<u^2>}{3}Q^2\right)$. The mean square displacement, $< u^2 >$, and its temperature dependence can be readily approximated from the phonon density of states [106,107]. If additional dynamical processes such as diffusion set in, the mean square displacement increases, further decreasing the observed elastic intensity below the value predicted by the DWF of harmonic dynamics. An extension of this mode is the inelastic fixed window scan (IFWS) [126], recently introduced and currently available only at IN16b at the ILL. During this scan the goal is to measure as long as possible at a chosen energy transfer, *i.e.* at a constant Doppler velocity. During a single temperature ramp, different fixed windows can be cycled. The advantage of the fixed window scans is that they provide an overview on the sample dynamics with good statistics in relatively short measurements.

- Energy transfer spectra: a full energy transfer spectrum at fixed temperature can be obtained periodically modulating the incident energy, by moving the Doppler monochromator with a sinusoidal velocity profile. The neutron counts from the detectors are sorted into a spectrum as a function of the energy transfer by a multichannel analyser. The energy transfer range is typically limited to a few tens/hundreds of μeV [124, 127].

For the investigations of proton dynamics in proton conducting oxides, the

high resolution of NBS spectrometers can provide information at longer times than a ToF instrument, possibly enabling the observation of the long-range diffusion. Moreover, the quick overview on the temperature dependence of the motion given by the FWSs can add useful information, for example identifying the onset of a specific process or enabling an accurate estimation of the mean square displacement and its temperature dependence. In this context, Paper V reports on a study carried out at the NBS spectrometer IN16b at ILL on 10Y:BZO and 10Sc:BZO, and on a series of In-doped samples with a doping level ranging from 10% to 25%. The high resolution together with a Q-range up to *ca* 2 Å^{-1}, and the combination of FWSs and full spectra in the range $\pm$ 25 μeV were the key to get insights into the details of the proton diffusion and its dependence on the dopant atom and concentration.

4.3 Neutron spin-echo spectroscopy

A crucial aspect in the inelastic spectrometers described so far is that the improvement of the instrumental resolution, and therefore the maximum time scale that can be probed, can be achieved only at the expense of the intensity. The NSE technique was introduced to overcome this conflict, pushing the achievable time scales towards longer values [128]. As a result, one of the main strengths of NSE is its wide dynamical range, as evidenced by Figure 4.1. An additional peculiarity of NSE is that it directly provides data in the (ϑ, t) phase space [129].

In NSE, the velocity change of incident and scattered neutrons are encoded using the Larmor precession of the neutron spin in an external magnetic field, which is used as an "internal clock" [128–130]. A polarized neutron beam enters in a magnetic field region and subsequently, after the scattering at the sample, into another with the same length and a magnetic field of the same strength but opposite direction. At the quasielastic limit, where the energy transfers

are small compared with the incoming energy, the total precession angle, ϕ, is directly proportional to the energy transfer and the NSE Fourier time t, which can be written as

$$t = \frac{\hbar\gamma}{m_{\mathrm{n}} v^3} \int B \, \mathrm{d}l, \tag{4.4}$$

where γ is the gyromagnetic ratio of the neutron, m_{n} is the neutron mass, v is the neutron velocity, $\hbar$ is the reduced Planck constant, and $\int B \, \mathrm{d}l$ is the field integral, *i.e.* the integral of the external magnetic field B along the neutron trajectory. The quasielastic condition is fulfilled for the whole dynamic range covered in a NSE experiment. The measured polarization in NSE is thus:

$$P = \langle \cos\phi \rangle = \frac{\int \cos(\omega\, t) S(Q,\omega) \mathrm{d}\omega}{\int S(Q,\omega) \mathrm{d}\omega}. \tag{4.5}$$

It follows that the real part of the normalised intermediate scattering function is directly obtained. As a result, the instrumental resolution, that is convoluted with the dynamic structure factor in an experiment in the (Q,ω) phase space, is here simply multiplied. The signal from a totally elastic scatterer is measured and used to divide the signal from the data [128, 130].

The use of polarized neutrons allows the estimation of the nuclear and spin-incoherent scattering relative weights. In the materials investigated for this thesis they can very well approximate the coherent and incoherent scattering relative weights, here indicated as $I_{\mathrm{coh}}(Q, t=0) = S_{\mathrm{coh}}(Q)$ and $I_{\mathrm{inc}}(Q, t=0) = S_{\mathrm{inc}}(Q)$, respectively. The normalised intermediate scattering function can be hence written as [128]:

$$\frac{I(Q,t)_{\mathrm{NSE}}}{I(Q,t=0)_{\mathrm{NSE}}} = \frac{I_{\mathrm{coh}}(Q,t) - \frac{1}{3} I_{\mathrm{inc}}(Q,t)}{S_{\mathrm{coh}}(Q) - \frac{1}{3} S_{\mathrm{inc}}(Q)}, \tag{4.6}$$

From Eq. 4.6, we note that if one of the components shows no dynamics, the complete decay of the NSE intermediate scattering function takes values that

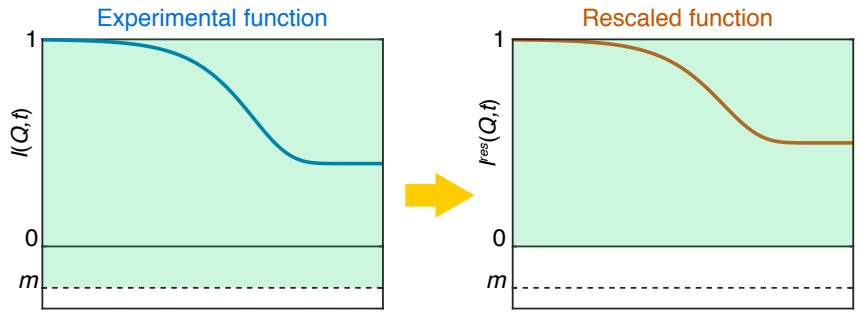

Figure 4.4: Schematic representation of an NSE $I(Q,t)$ with an exponential decay to a complete decay level m. Such a value depends on the relative weights of coherent and incoherent scattering, that is by the composition of the sample. To compare the NSE $I(Q,t)$ (left side of the figure), which has therefore its codomain (green area) in [m,1], with data from models or other experiments, the function has to be rescaled into the codomain [0,1]. The rescaled function is shown in the right part of the figure. This procedure is explained in details in Paper I.

depend on the relative weights of coherent and incoherent scattering, *i.e.* on the sample composition, and these values can be also negative. This has to be taken into account to compare the NSE data from different samples, with different coherent/incoherent ratios, but also with the $I(Q,t)$ that can be derived, for example, by Fourier transforming the dynamic structure factor obtained with a ToF or NBS spectrometer for the same sample. In the case of the measurements presented in Paper I on hydrated Y- and Sc-doped barium zirconates at the IN11 [124] spectrometer at the ILL, considerations on the different contributions and an accurate evaluation of the hydrogen concentration in the materials allowed the calculation of the level of an hypothetical complete decay of the $I(Q,t)$ within the experimental time window. This procedure is summarised in Figure 4.4 and described in detail in Paper I.

NSE was only fairly recently applied for the first time to the study of the proton dynamics in barium zirconates [76]. It clearly offers a unique possibility to map a wide dynamical region, as shown in Paper I where measurements exploring the dynamics in 10Y:BZO and 10Sc:BZO in a time region between 5 ps

and 1.3 ns and within a momentum transfer range of 0.7-1.2 $Å^{-1}$ are presented. However, it has to be noted that the different effect on the polarization of the coherent and incoherent contributions has important consequences in the application of NSE on proton conductors. These systems are prevalently incoherent scatterers, and the -1/3 factor in polarization decreases the statistical accuracy. Moreover, the coherent scattering intensity changes strongly with Q, as mentioned in Section 3.1. If at some Q-values the incoherent contribution is about three times higher than the coherent one, the resulting polarization is zero at those values, making the measurement difficult. A multidetector option helps to compensate for the low intensity. It also permits to have a quick overview of the coherent/incoherent ratios over a wide range of Q-values and therefore to possibly select the best region for the measurement. This option was used during the experiment described in Paper I, for which it was exploited the 30° wide-angle detector of the IN11-C setup [124, 128], shown in Figure 4.5.

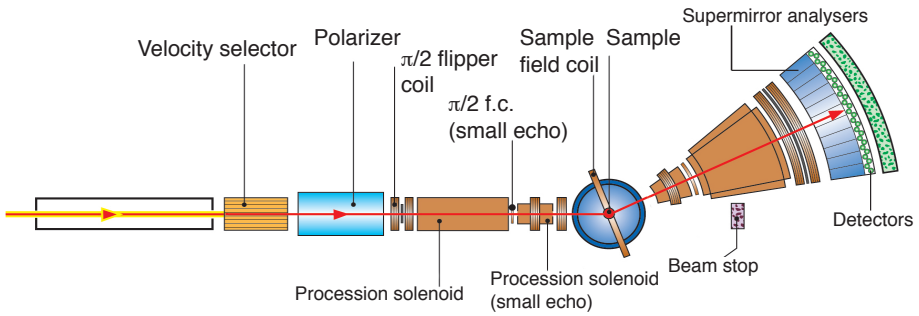

Figure 4.5: Schematic representation of the IN11 NSE spectrometer at ILL, in its configuration exploiting the 30°wide-angle detector. Figure courtesy of the ILL.

4.4 Neutron diffraction with polarization analysis

For a correct interpretation of the dynamics data, obviously a good sample characterization is very important. For example, an accurate evaluation of the hydrogen content in proton conducting oxides is needed for the calculation of the level of the complete decay of the intermediate scattering function in NSE, as described above. In this respect, polarized neutron diffraction (pND) is a useful tool, having the advantage that the hydrogen concentration can be provided on the very same samples (previously or subsequently) used for QENS/INS investigations.

Figure 4.6 shows the layout of the diffuse scattering spectrometer D7 [118, 124] at the ILL, at which the diffraction measurements with polarization analysis presented in this thesis were carried out. In such an instrument, the neutron incident wavelength (3.1, 4.8 or 5.8 Å) is selected by the monochromator, and the beam is polarized in the z-direction. The neutrons then pass through a Mezei spin-flipper, a device that project the direction of the polarization onto an arbitrary field axis, which is "of" when measuring non-spin-flip cross-sections, and "on" when measuring spin-flip cross-sections. The polarization of neutrons is set into the x-, y- or z-direction using three orthogonal magnetic coils situated at the sample position. After being scattered from the sample, the neutrons are analysed for their final spin state, and detected using the three multi-analyser/detector banks.

The spin incoherent component can be used to estimate the hydrogen concentration of the materials. The advantage of using pND to this aim is mainly in its non-destructiveness, so that the estimation can be done on the very same sample used for other measurements without the need to manipulate the sam-

ples, therefore avoiding possible deterioration of the samples, such as variations of the hydration level. This is explained in more detail in Paper I, III and VI, where the characterization of the hydration level of the samples using pND is presented. Moreover, in Paper II and III the changes in the position and shape of the Bragg peaks as a function of the In and H concentrations were used to infer information regarding the modifications of the local structure induced by the acceptor doping and hydration.

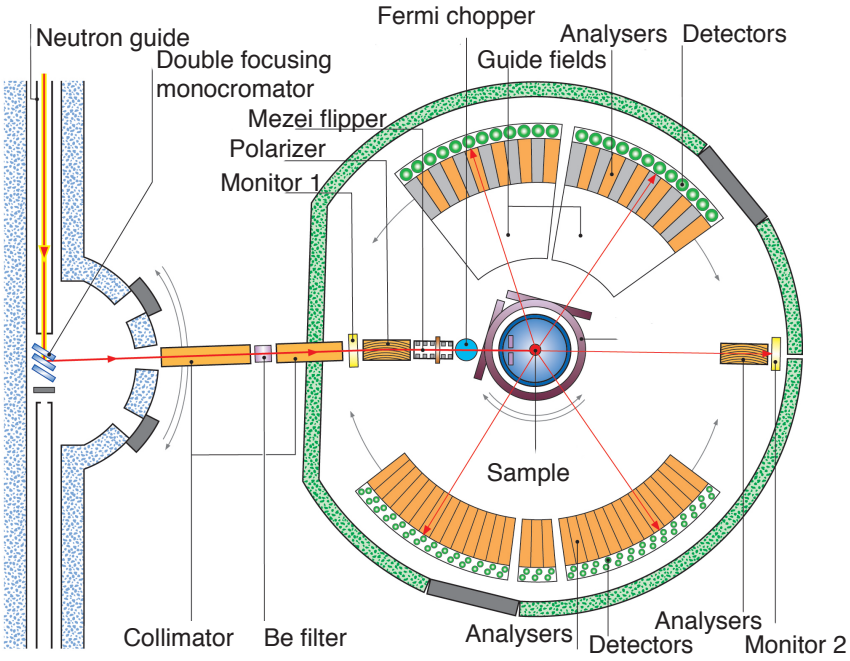

Figure 4.6: Schematic representation of the diffuse scattering spectrometer D7 at ILL. Figure courtesy of the ILL.

Chapter 5

Summary of the appended papers

As mentioned in the preceding chapters, this thesis builds on detailed neutron scattering studies of the mechanistic details of proton dynamics, extending from vibrational to localized and long-range diffusion, in acceptor doped barium zirconate based proton conductors, with focus onto the effect of different dopant atoms and doping levels. In order to obtain such information, a wide portion of the $Q-E$ space needed to be explored. This was obtained by properly combining different instruments and setups for the QENS measurements, as summarised in Figure 5.1. Thermogravitric analysis (TGA), pND, IR spectroscopy, INS, x-ray diffraction (XRD), scanning electron microscopy (SEM) and energy dispersive x-ray analysis (EDX) were used as complementary techniques in order to gain information regarding hydration level, local structural properties, chemical composition and vibrational dynamics.

Papers I-II: investigations on the effect of the dopant atom

The aim of the study reported in Paper I was to relate the difference in macroscopic conductivity of hydrated $BaZr_{0.9}M_{0.1}O_{2.95}$ (M= Y and Sc) (*cfr.* 2) with differences in the atomic-scale proton dynamics, by exploiting the wide dy-

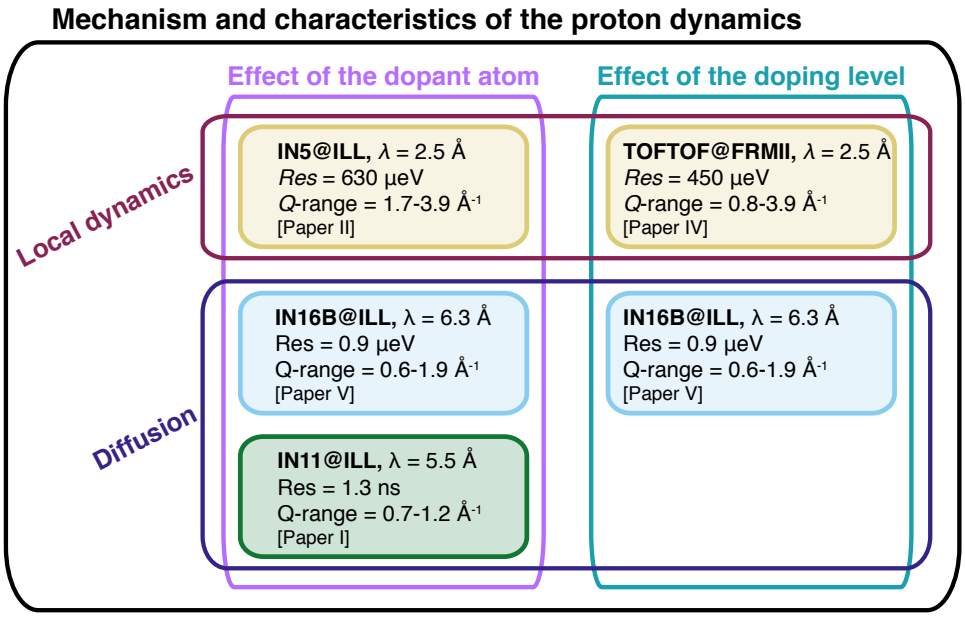

Figure 5.1: Overview of the QENS investigations presented in the appended papers. For each QENS experiment the instrument, the incident neutron wavelength λ, the Q-range and the resolution are indicated.

namical range (time range of 5 ps–1.3 ns and a momentum transfer range of 0.69–1.23 Å^{-1}) probed by the NSE spectrometer IN11 at the ILL. To enhance the statistics, limited by the loss of polarization due to the predominantly incoherent nature of the signal (*cfr* Section 4.3), data were summed over the entire Q-range, thus obtaining an average Q-value of 0.96 Å^{-1}. In order to carry out a Q-dependent analysis, the recording time of the signal at the highest temperature, 546 K, was increased, enabling the split of the data into three Q-groups at 0.77, 0.99, and 1.17 Å^{-1}. The hydration degree of the samples was carefully measured with TGA and pND, the latter introduced for the first time for the estimation of hydration degree in proton conducting oxides. In addition, IR spectroscopy was used to obtain insights into the nature of proton sites.

At the time scale accessible by the measurements, results showed proton motions for temperatures above 300 K, with no strong dependence on the type of dopant atom. The stretched profile of the NSE intermediate scattering func-

tions (Figure 5.2) were interpreted as the result of a distribution of different time scales reflecting dynamics in the wide distribution of locally different proton configurations shown by the IR measurements, rather than associated with dynamics characterized in terms of a unique relaxation time featuring a single microscopic relaxation process with a well-defined activation energy. These findings were therefore in agreement with previous computational studies [57] and IR and Raman data [54,131] and supported the heterogeneous scenario [92] described in Section 2.1.3. Due to such a stretched profile, the footprint of the proton dynamics seemed to be extended to much longer times, towards the time domain of oxygen diffusion, making the time window probed by the IN11 experiment too narrow for a reliable parametrization of the intermediate scattering function. However, the hypothesis of a plateau in the intemediate scattering function arising from immobile hydrogen atoms was also considered. Indeed, both TGA and pND were consistent in showing a peculiarly high hydrogen concentration, which exceeded the theoretical maximum and was possibly related to the presence of immobile hydrogenated species as impurities. Such an observation opened questions regarding the possible impact of this extra hydrogen concentration on the proton dynamics. Moreover, the dynamics did not appear strongly dependent on the Q-value, in the probed, yet quite narrow, range. The need to extend the accessible Q-range while maintaining a similar time scale, in order to clarify if the motion was really localized or if the Q-independency was only apparent due to the limited Q-range, was therefore suggested. Further, with a comparison as explained in Chapter 4, it was shown that at short time scale the NSE signal could be consistently complemented by results derived from previous investigations on the same compunds with ToF neutron spectroscopy [70].

In such a previous study, 10% Y- and Sc-doped barium zirconates were investigated in the ps region, identifying local dynamics with onset around 300 K

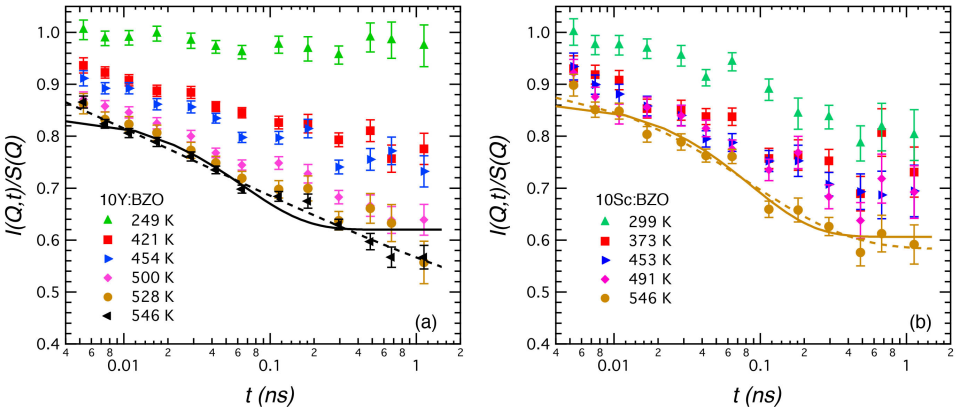

Figure 5.2: Temperature dependence of the normalized intermediate scattering function, $I(Q,t)/S(Q)$, at the average Q of 0.96 Å^{-1} for (a) hydrated $BaZr_{0.9}Y_{0.1}O_{2.95}$ (10Y:BZO) and (b) hydrated $BaZr_{0.9}Sc_{0.1}O_{2.95}$ (10Sc:BZO). Solid lines are free fits to the 546 K data using single exponential functions; dashed lines are free fits to the 546 K data using stretched exponential functions.

[70]. The narrow Q-range, up to *ca* 2.0 Å^{-1}, was however a limiting factor for the determination of the type of relaxation process. In the investigation reported in Paper II, the very same samples as in Paper I were therefore studied at a time scale comparable with that of the preceding ToF experiment, but in the more extended Q-range of *ca* 1.7–3.9 Å^{-1}, at the IN5 ToF spectrometer. The study in such a Q-range was indeed suggested to be determinant to unambiguously discriminate between the geometry related to the two fundamental steps of the Grotthuss mechanism. In accordance to the approach proposed in the previous study, the model for jump displacements over N equivalent sites located on a circle with radius r was used [113, 132–135]. With N= 2 the model is meant to approximate the proton transfers between neighbouring oxygens, and with N= 4 the -OH reorientations. The main equations of the model and their application to the experimental data are described in the Supporting Information (SI) of Paper II.

The results showed the presence of localized proton dynamics, similar for

the two materials and characterised by a quasielastic signal which broadens with increasing temperature, with activation energies of the order of 100 meV. As described, localized dynamics with similar characteristics were largely interpreted as -OH reorientations in previous studies, mainly on the basis of the low activation energy. However, it was also underlined how in barium zirconates the activation energies for -OH reorientations are not supposed to be much lower or even lower at all of those of transfers, on the basis of computational studies [57, 60]. Considering both the processes is therefore justified, and the IN5 results showed that the geometry of the dynamics is indeed compatible with both transfers and reorientation, with jump lengths or O-H distances well in line with the structural parameters and bondlengths as reported in literature [54, 87, 101, 136, 137]. Moreover, building on the NSE results of Paper I, the heterogeneous scenario was also tested. To do so, computational data from literature [57] were re-elaborated in order to make them directly comparable with the present experiment. The distribution of energy barriers and frequencies resulting by different proton sites as calculated by Björketun and coworkers were used to compute the components expected within the framework of the same models used for the IN5 data [57]. The calculated components are relative to the processes graphically summarised in the insert of Figure 5.3. The comparison of the so-derived components with the experimental ones (Figure 5.3) suggested that the dynamics probed by the QENS experiment could comprise contributions from several proton transfers and -OH rotational motions taking place in different types of local proton sites. The presence of a large fraction of immobile protons was also detected, in accordance with previous studies on similar materials [53, 69].

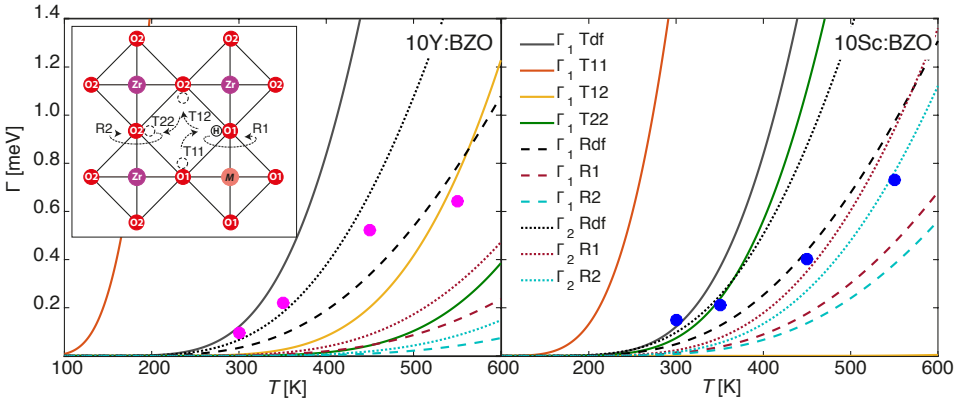

Figure 5.3: Comparison of the full widths at half maximum of the experimental components Γ, indicated with bullets with results from computational studies. The lines represent the calculated full widths at half maximum of the components derived for the relevant migration steps (see inset) using residence times obtained from DFT calculations [57] and the transition state theory, together with a jump over 2 or 4 sites models.

Papers III-IV: influence of doping and hydration levels on local structure and dynamics

Following these intriguing results, local structure and dynamics were then investigated with the aim to study how they are affected by the doping level. In Paper III, pND at D7 was used to characterize a series of In-doped samples with different doping/hydration levels (hydrated $BaZr_{1-x}In_xO_{3-x/2}$ with x= 0–27.5), in order to carefully determine the hydrogen content and identify eventual effects of the doping on the structure. The applicability of pND as a routinely complementary characterization technique for the QENS/INS studies on proton conducting perovskites is also discussed. Within the same, quick, measurement: (i) the hydrogen content was determined from the incoherent component, obtaining consistent values with those measured with TGA, and (ii) although limited by instrumental constraints, information on the structural modifications induced by the dopant could be inferred using the nuclear diffraction pattern. This last point would obviously profit from a possible future coupling of polar-

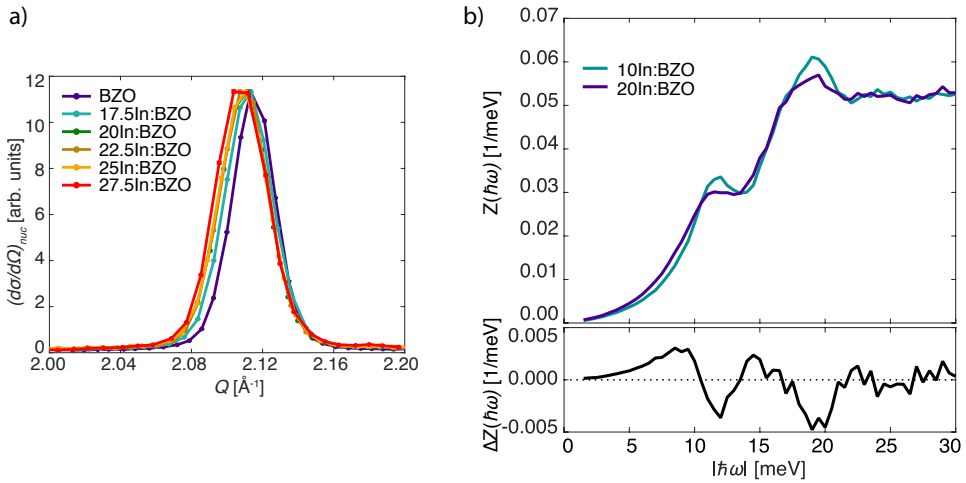

Figure 5.4: a) Evolution of the Bragg Peak 110 in the different samples, rescaled to the intensity of the BZO sample. Increasing the doping/hydration level, it is possible to note a shift towards lower angles and a broadening of the peak. b) Generalised density of states, $Z(\hbar\omega)$, for 10In:BZO and 20In:BZO. Data have been collected at the temperature of 350 K and normalized to the same number of vibrational states in the energy range 0−30 meV in the anti-Stokes side. Bottom panel: $\Delta Z(\hbar\omega) = Z_{\mathrm{20In:BZO}}(\hbar\omega) - Z_{\mathrm{10In:BZO}}(\hbar\omega)$.

ized neutrons with more powerful diffractometers. In the investigated samples, the evolution of the characteristics of the Bragg peaks as a function of doping and hydration level revealed a shift towards higher Q-values and an increase of the FWHM with increasing In concentration and hydration level, likely due to corresponding enlarged cells and increased disorder (Figure 5.4 a)). These results are in agreement with previous studies [54,84,88,89], complementing them at several intermediate In concentration values and on protonated (instead of deuterated) samples.

In Paper IV, such observations on the effect of the doping level on the local structure were related with the localized dynamics as probed by QENS/INS measurements carried out at TOFTOF on hydrated $BaZr_{1-x}In_xO_{3-x/2}$ ($x = 0.10$ and 0.20), with a similar setup as in Paper II.

The generalised density of states (Figure 5.4 b)) confirmed an increased

disorder and cell dimension associated with a higher doping level: for the 20%-doped sample, the optic phonon peaks are broadened and more vibrational states are present in the low-energy acoustic region. The analysis of the elastic and quasielastic signals disclosed a fraction of immobile protons and a fraction of protons showing localized dynamics, compatible with both transfers and reorientations, and also with a complex picture of several proton transfers and -OH reorientational motions contributing to the quasielastic component, thus confirming the results of Paper II. Higher doping concentration, *i.e.* bigger cell and more distorted structure, seems to favour faster local dynamics. Furthermore, the determining factor in causing the different responses of the transition rates seems to be given by the trial frequencies. Their qualitative trend as a function of the structural disorder resembled that of O-H bend frequencies, as reported by several IR and INS spectroscopy investigations of In-doped barium zirconates [54, 55, 85]. Considering that O-H bend modes are supposed to facilitate the -OH reorientations [57], the similar trends suggest a predominant role of these motions in the observed dynamics.

Paper V: modelling proton diffusion

Whereas the localized dynamics as a function of type and concentration of dopant ions were successfully modelled in Papers II and IV, the mechanism and the details of the long-range proton diffusion remained so far elusive. The NSE study reported in Paper I was mainly hindered by the limited Q-range, and the low resolution of the ToF experiments allowed to focus only onto the localized dynamics observable at the ps time scale. NBS measurements at the IN16b spectrometer at the ILL provided an excellent compromise, combining an energy resolution of less than 1 μeV, *i.e.* improved by more than 2 orders of magnitude in respect to the ToF studies of Papers II and IV and comparable with the NSE study of Paper I, and the signal from 7 different Q-values in a

range up to 1.9 Å^{-1}, *i.e.* sensibly extended in respect to the NSE study of Paper I. Such NBS investigations, reported in Paper V, were conducted on a series of 10%-doped samples with different dopant atoms (M= Y, In and Sc) and on a series of In-doped samples with different doping level (x= 0–25). Three different types of measurements were combined: EFWS, IFWS at 2 μeV, and full spectra in the energy range of $\pm$ 25 μeV.

With the EFWS the onset temperature of the dynamical processes T_c was accurately identified. It was found that T_c increases from less than 200 K in M = Sc, Y and In with x = 0.1 up to about 320 K in M = In with x = 0.25 along the sequence of x. The IFWS, Figure 5.5, confirmed these trends, showing moreover that the fraction of mobile protons increases as a function of increasing temperature, as well as of increasing x. In the 10%-doped samples, it increases along the series Sc, Y and In, with a stronger difference between Y and In. The Q-dependencies of the inelastic scans suggest proton diffusion rather than localized motions, especially for the low-doped samples, for which the features in the scans are clearer due to the onset at lower temperatures. An additional

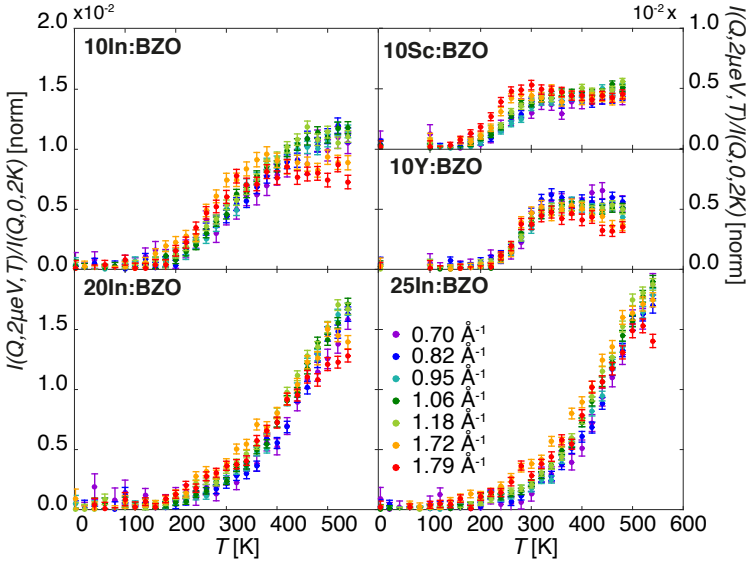

Figure 5.5: Intensities measured with the IFWS mode at 2 μeV.

increase of inelastic intensities at high T is visible in the low-doped samples. This feature points towards multi-process relaxations, therefore in accordance with the NSE study reported in Paper I. The probed T-window (up to 550 K) is not sufficient to establish the behaviour for the In-doped samples with higher x values. The NBS investigations also helped in clarifying the role of the exceeding hydrogen concentration on the proton dynamics, question that emerged from Paper I. Their influence on the observed dynamics seemed minor, and they are mainly manifested as immobile species in the dynamical and temperature window accessible within the experimental setup. The mechanism of the diffusion came out more clearly from the analysis of the full spectra. There were identified Q-independent but T-dependent elastic intensities, associated with immobile protons, and Q- and T-dependent quasielastic widths presenting the signatures of thermal activated jump-diffusion. Three well-established jump diffusion models were tested, as reported in Figure 5.6: Hall and Ross [138], Singwi and Sjölander [139], and Chudley and Elliot [79], all described in the SI of Paper V. The best agreement was found with the Chudley-Elliot model, with a jump length of *ca* 3 Å, which roughly corresponds to the O-O distances in

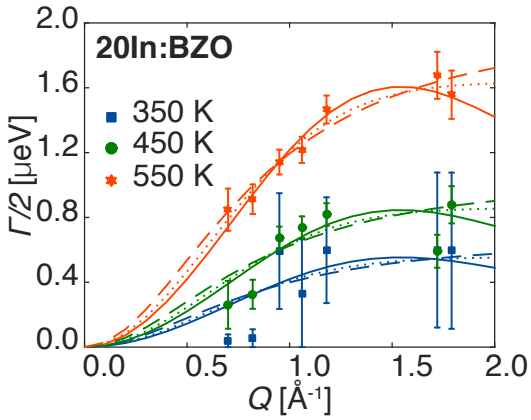

Figure 5.6: Fit of the widths of the quasielastic component of $BaZr_{0.8}In_{0.2}O_3H_{0.2}$, 20In:BZO, according with jump diffusion models: Chudley-Elliot (solid lines), Singwi-Sjölander (dashed lines) and Hall-Ross (dotted lines).

the materials, in accordance with the studies of Hempelmann's group [69, 73]. The derived diffusion coefficients presented values of *ca* 3 Å^2/ns at 550 K, thus compatible with those from QENS and conductivity measurements for similar materials [3, 53, 56, 73, 77, 86, 92]. In accordance with the behaviour of T_c, the activation energy E_a increases from about 40 to 120 meV from $x = 0.1$ to 0.2. The established values are lower than what generally reported for proton diffusion in similar materials, as described in Section 2.1.3, possibly suggesting other processes, beyond the NBS window, which limit the conductivity. However, the activation energies are in good agreement with the values proposed for $BaCe_{0.8}Y_{0.2}H_{0.2}O_3$ and $BaZr_{0.9}Y_{0.1}H_{0.1}O_3$ below 700 K by Braun and coworkers [75, 77].

Chapter 6

Conclusions and outlook

To conclude, this thesis provides new fundamental understanding of atomic-scale dynamics of protons in proton conducting barium zirconates, ranging from the fast vibrational motions of protons through localized proton motions to long-range diffusion. With respect to the localized dynamics, it was found to be associated with low activation energies and compatible with both proton transfer between two adjacent oxygens and rotation of the -OH group. Moreover, it was shown also the agreement with a complex scenario, in which the signal results as the average of several contributions given by such proton motions related to an heterogeneity of proton sites. The trend as a function of increased distortions induced by higher doping concentration suggests a predominance of -OH rotational motions in the observed dynamics. A key result is also that whereas no strong dependence could be established for different dopant ions, higher doping levels seem to favour faster local dynamics. Evidences for multi-process relaxations were also found regarding long range proton diffusion for the 10%-doped samples, both from the NSE and the NBS investigations. The geometry of the dynamics was identified as a jump diffusion in accordance with the Chudley-Elliot model, with a characteristic jump distance of 3 Å. A central result is that

the effect of the doping level is manifested in higher onset temperatures and larger activation energies for increasing doping concentration, as well as with a reduced relative fraction of immobile protons. Overall, the new results hence contribute in building a detailed knowledge of proton conduction mechanism in proton conducting oxides. Besides being of considerable fundamental interest, such knowledge is of relevance for the development of design criteria for new proton conductors with optimized proton conductivity, suitable for applications in important technological environmentally friendly devices, such as next generation intermediate- and low-temperature SOFCs. The results shown in this thesis can be therefore expected to be of significant interest to the large community of scientists active in research and development of proton conducting materials.

With a view to the future, the new results also suggest possible ways for further advancements. Whereas the focus in this thesis was onto the low-T regime (below 600 K), a rather unexplored temperature region with respect to QENS experiments on proton conducting oxides, complementary insights should come from systematic QENS investigations at $T > 600$ K. For example, it should be possible to clarify the presence of the postulated crossover from a low- to high-T behaviour of the proton dynamics [75, 77]. Further, the processes observed by NBS in the 10%-doped samples towards high-T could be characterized, and it could be verified if the characteristics of the dynamics of the highly doped samples are similar but progressively shifted to higher T.

It was here shown that the combination of many neutron scattering instruments, with different resolution and dynamical range, is crucial to get a comprehensive view over the (complex) proton conduction mechanism. In this respect, instrumentation developments are of obvious interest. For example, improved-resolution NBS spectrometers [140] would allow to explore dynamics beyond 1 ns in a relatively large Q-range. Furthermore, the need of a thoroughly

characterization of the samples is also clear and, in this regard, important information about the hydrogen concentration was obtained in this project from pND measurements. Extended systematic studies with this technique at different temperatures and comparing dry and hydrated materials with different doping and hydration levels might bring new insights regarding the effect of the acceptor doping and hydration procedures. The use of polarized neutrons for the investigation of proton conducting materials might be further extended to inelastic measurements, possibly representing a relevant improvement for future studies, for example allowing to explore the incoherent dynamics in the Q-ranges affected by the presence of the Bragg peaks and to clearly distinguish between collective motions and self-dynamics. Finally, it would be of high interest to investigate the behaviour of proton conducting oxides in conditions similar to those in a fuel cell under operation. In this respect, progresses in technical devices allowing so are intriguing. For example, it has been developed a cell that permits QENS studies at high temperatures in a controlled vapour environment [141]. Such *in situ* studies may also contribute to a deeper comprehension of the hydration process in these materials, which is also not fully understood [26, 65, 66].

Appendix A

Hydration/dehydration equilibrium

A.1 Concentration of protonic defects

To derive the theoretical concentration of protonic defects as a function of temperature, we start from Eq. 2.1, reported here again for convenience:

$$H_2O(g) + V_O^{\bullet\bullet} + O_O^{\times} \rightleftharpoons 2(OH_O^{\bullet}), \tag{A.1}$$

where $V_O^{\bullet\bullet}$ is the oxygen vacancy, $O_O^{\times}$ is the oxide ion, and $OH_O^{\bullet}$ is the hydroxyl ion. Assuming an ideal behaviour of all the species involved, the equilibrium constant is given by [142]:

$$K = \frac{[OH_O^{\bullet}]^2}{[V_O^{\bullet\bullet}][O_O^{\times}]p_w}. \tag{A.2}$$

The partial pressure of vapour p_w can be calculated using Dalton law, multiplying the molar fraction of vapour x_w with the total pressure p: $p_w = x_w p$ [142]. If no ideal behaviour is assumed, activities and fugacity should be used instead of concentrations and pressure [142]. The temperature dependence of the equi-

librium constant is given by [142]:

$$K = \exp\left(\frac{-\Delta G^0}{k_B T}\right), \tag{A.3}$$

where ΔG^0 is the standard-state[1] Gibbs energy of the reaction and k_B is the Boltzmann constant. The site restriction gives:

$$N_{\mathrm{O}} = [\mathrm{OH}_{\mathrm{O}}^{\bullet}] + [V_{\mathrm{O}}^{\bullet\bullet}] + [\mathrm{O}_{\mathrm{O}}^{\times}], \tag{A.4}$$

where N_{O} is the number of oxygen sites per formula unit, which is 3 for a perovskite. Assuming a single acceptor dopant M, and that only vacancies and protons compensate for the dopant, the charge neutrality condition gives:

$$0 = 2[V_{\mathrm{O}}^{\bullet\bullet}] + [\mathrm{OH}_{\mathrm{O}}^{\bullet}] - [M]. \tag{A.5}$$

We thus arrive to Eq. 2.2 [44], reported here again for convenience :

$$[\mathrm{OH}_{\mathrm{O}}^{\bullet}] = N_{\mathrm{O}} \frac{K'}{K'-4}\left[1 - \sqrt{1 - \frac{K'-4}{K'}\left(\frac{2[M]}{N_{\mathrm{O}}} - \frac{[M]^2}{N_{\mathrm{O}}^2}\right)}\right], \tag{A.6}$$

where $K' = p_w K$. The treatment can be further refined by considering the effective acceptor dopant concentration, S [86]. The equation 2.2 is therefore slightly modified and, with $N_{\mathrm{O}} = 3$, becomes [86]:

$$[\mathrm{OH}_{\mathrm{O}}^{\bullet}] = \frac{3K' - \sqrt{K'(9K' - 6K'S + K'S^2 + 24S - 4S^2)}}{K'-4} \tag{A.7}$$

[1] 1 atm, 298.15 K

A.2 Details of the calculation of the hydration curves

Hydration standard-state enthalpies ΔH^0 and entropies ΔS^0 were taken from Ref. [86], and used to calculate $\Delta G^0 = \Delta H^0 - T\Delta S^0$ [142]. To approximate the conditions in the laboratory, a relative humidity (R.H.) value of 40%, a typical value of a quite dry indoor ambient, was chosen. The vapour partial pressure was derived from the relative humidity:

$$R.H. = \frac{p_w}{p_w^*}, \tag{A.8}$$

where p_w^* is the saturated vapour pressure, calculated using Clausius-Clapeyron equation [142]. The vapour partial pressure for hydration conditions was taken from Ref. [143].

For simulating the conditions in a tightly closed cell, it was considered to be sealed at ambient conditions (p= 1 atm and temperature of 25 °C) and a relative humidity of 40%. Moistened air has been considered a perfect gas at these conditions. The total pressure in the cell during heating was calculated using van der Waals coefficients and second virial expansion, to take into account possible deviations from ideality at higher pressure [142]. Van der Waals coefficients were estimated considering a mixture of vapour and dry air (which was approximated by a composition of 80% N_2, 20% O_2), according to the calculated x_w. In a more rigorous treatment, vapour fugacity instead of vapour pressure could be used [142]. However, this was considered a sufficiently good approximation for the purpose in this thesis.

Bibliography

[1] J. A. Kilner and M. Burriel, "Materials for intermediate-temperature solid-oxide fuel cells," *Annual Review of Materials Research*, vol. 44, no. 1, pp. 365–393, 2014.

[2] L. Malavasi, C. A. J. Fisher, and M. S. Islam, "Oxide-ion and proton conducting electrolyte materials for clean energy applications: Structural and mechanistic features," *Chemical Society Reviews*, vol. 39, no. 11, pp. 4370–87, 2010.

[3] K.-D. Kreuer, "Proton-conducting oxides," *Annual Review of Materials Research*, vol. 33, no. 1, pp. 333–359, 2003.

[4] K.-D. Kreuer, "Proton conductivity: Materials and applications," *Chemistry of Materials*, vol. 8, no. 3, pp. 610–641, 1996.

[5] F. M. Ernsberger, "The nonconformist ion," *Journal of the American Ceramic Society*, vol. 66, no. 11, pp. 747–750, 1983.

[6] P. Knauth and M. L. Di Vona, "Inorganic solid proton conductors," in *Solid State Proton Conductors: Properties and Applications in Fuel Cells*, pp. 371–397, 2012.

[7] C. J. T. de Grotthuss, "Mémoire sur la décomposition de l'eau et des corps qu'elle tient en dissolution à l'aide de l'électricité galvanique," *Annales de Chimie*, vol. LVII, p. 54, 1806.

[8] J. W. Phair and S. P. S. Badwal, "Review of proton conductors for hydrogen separation," *Ionics*, vol. 12, no. 2, pp. 103–115, 2006.

[9] Y. Sone, P. Ekdunge, and D. Simonsson, "Proton conductivity of Nafion 117 as measured by a four-electrode AC impedance method," *Journal of The Electrochemical Society*, vol. 143, no. 4, p. 1254, 1996.

[10] M. G. Shilton and A. T. Howe, "Rapid H^+ conductivity in hydrogen uranyl phosphate-A solid H^+ electrolyte," *Materials Research Bulletin*, vol. 12, no. 7, pp. 701–706, 1977.

[11] S. M. Haile, D. A. Boysen, C. R. I. Chisholm, and R. B. Merie, "Solid acids as fuel cell electrolytes," *Nature*, vol. 410, no. 6831, pp. 910–913, 2001.

[12] M. Marrony, *Proton-conducting Ceramics*. New York: Pan Stanford, 1 ed., 2015.

[13] T. Ishihara, ed., *Perovskite Oxide for Solid Oxide Fuel Cells*. Fuel Cells and Hydrogen Energy, Boston, MA: Springer US, 2009.

[14] K.-D. Kreuer, A. Rabenau, and W. Weppner, "Vehicle mechanism, a new model for the interpretation of the conductivity of fast proton conductors," *Angewandte Chemie International Edition in English*, vol. 21, no. 3, pp. 208–209, 1982.

[15] U.S. Energy Information Administration (EIA), "https://www.eia.gov/," 2017.

[16] E. D. Wachsman and K. T. Lee, "Lowering the temperature of solid oxide fuel cells," *Science (New York, N.Y.)*, vol. 334, no. 6058, pp. 935–9, 2011.

[17] E. Wachsman, T. Ishihara, and J. Kilner, "Low-temperature solid-oxide fuel cells," *MRS Bulletin*, vol. 39, no. 09, pp. 773–779, 2014.

[18] D. J. L. Brett, A. Atkinson, N. P. Brandon, and S. J. Skinner, "Intermediate temperature solid oxide fuel cells," *Chemical Society Reviews*, vol. 37, no. 8, pp. 1568–78, 2008.

[19] L. Carrette, K. A. Friedrich, and U. Stimming, "Fuel cells: Principles, types, fuels, and applications," *ChemPhysChem*, vol. 1, no. 4, pp. 162–193, 2000.

[20] E. Fabbri, A. Magrasó, and D. Pergolesi, "Low-temperature solid-oxide fuel cells based on proton-conducting electrolytes," *MRS Bulletin*, vol. 39, no. 09, pp. 792–797, 2014.

[21] B. C. Steele and A. Heinzel, "Materials for fuel-cell technologies," *Nature*, vol. 414, no. 6861, pp. 345–52, 2001.

[22] M. Karlsson, "Perspectives of neutron scattering on proton conducting oxides," *Dalton Transactions*, vol. 42, no. 2, pp. 317–29, 2013.

[23] T. Norby, "The promise of protonics," *Nature*, vol. 410, no. 6831, pp. 877–878, 2001.

[24] N. Mohammad, A. B. Mohamad, A. A. H. Kadhum, and K. S. Loh, "A review on synthesis and characterization of solid acid materials for fuel cell applications," *Journal of Power Sources*, vol. 322, pp. 77–92, 2016.

[25] O. Naumov, S. Naumov, R. Flyunt, B. Abel, and A. Varga, "Fast degradation for high activity: Oxygen- and nitrogen-functionalised carbon nan-

otubes in solid-acid fuel-cell electrodes," *ChemSusChem*, vol. 9, no. 23, pp. 3298–3306, 2016.

[26] T. Norby, M. Widerøe, R. Glockner, and Y. Larring, "Hydrogen in oxides," *Dalton Transactions*, no. 19, pp. 3012–8, 2004.

[27] D. G. Thomas and J. J. Lander, "Hydrogen as a donor in zinc oxide," *The Journal of Chemical Physics*, vol. 25, no. 6, pp. 1136–1142, 1956.

[28] D. A. Shores and R. A. Rapp, "Hydrogen ion (proton) conduction in thoria-base solid electrolytes," *Journal of The Electrochemical Society*, vol. 119, no. 3, p. 300, 1972.

[29] E. Fabbri, D. Pergolesi, and E. Traversa, "Materials challenges toward proton-conducting oxide fuel cells: A critical review," *Chemical Society reviews*, vol. 39, no. 11, pp. 4355–4369, 2010.

[30] M. Widerøe, N. Kochetova, and T. Norby, "Transport numbers from hydrogen concentration cells over different oxides under oxidising and reducing conditions," *Dalton Transactions*, vol. 0, no. 19, p. 3147, 2004.

[31] R. Haugsrud and C. Kjølseth, "Effects of protons and acceptor substitution on the electrical conductivity of La_6WO_{12}," *Journal of Physics and Chemistry of Solids*, vol. 69, no. 7, pp. 1758–1765, 2008.

[32] M. Nagao, T. Kamiya, P. Heo, A. Tomita, T. Hibino, and M. Sano, "Proton conduction in In^{3+}-doped SnP_2O_7 at intermediate temperatures," *Journal of The Electrochemical Society*, vol. 153, no. 8, pp. A1604–A1609, 2006.

[33] T. Anfimova, T. Lie-Andersen, E. P. Jensen, C. B. Prag, U. G. Nielsen, D. R. Sørensen, E. M. Skou, E. Christensen, N. J. Bjerrum, and Q. Li, "The effect of preparation method on the proton conductivity of indium doped tin pyrophosphates," *Solid State Ionics*, vol. 278, pp. 209–216, 2015.

[34] R. Haugsrud and T. Norby, "Proton conduction in rare-earth ortho-niobates and ortho-tantalates," *Nature Materials*, vol. 5, no. 3, pp. 193–196, 2006.

[35] Y. Larring, "Protons in rare earth oxides," *Solid State Ionics*, vol. 77, pp. 147–151, 1995.

[36] T. Shimura, M. Komori, and H. Iwahara, "Ionic conduction in pyrochlore-type oxides containing rare earth elements at high temperature," *Solid State Ionics*, vol. 86-88, pp. 685–689, 1996.

[37] T. Takahashi and H. Iwahara, "Solid-state ionics - protonic conduction in perovskite type oxide solid-solutions," *Revue De Chimie Minerale*, vol. 17, no. 4, pp. 243–253, 1980.

[38] N. Taniguchi, K. Hatoh, J. Niikura, T. Gamo, and H. Iwahara, "Proton conductive properties of gadolinium-doped barium cerates at high temperatures," *Solid State Ionics*, vol. 53-56, pp. 998–1003, 1992.

[39] G. Zhang and D. M. Smyth, "Protonic conduction in $Ba_2In_2O_5$," *Solid State Ionics*, vol. 82, no. 3-4, pp. 153–160, 1995.

[40] T. Hashimoto, Y. Inagaki, A. Kishi, and D. Masayuki, "Absorption and secession of H_2O and CO_2 on $Ba_2In_2O_5$ and their effects on crystal structure," *Solid State Ionics*, vol. 128, no. 1-4, pp. 227–231, 2000.

[41] M. De Graef and M. E. McHenry, *Structure of Materials an Introduction to Crystallography, Diffraction and Symmetry.* Cambridge: Cambridge University Press, 1 ed., 2007.

[42] V. M. Goldschmidt, "Die gesetze der krystallochemie," *Naturwissenschaften*, vol. 14, no. 21, pp. 477–485, 1926.

[43] T. Norby and Y. Larring, "Concentration and transport of protons in oxides," *Current Opinion in Solid State and Materials Science*, vol. 2, no. 5, pp. 593–599, 1997.

[44] J. B. Nyman, E. E. Helgee, and G. Wahnström, "Oxygen vacancy segregation and space-charge effects in grain boundaries of dry and hydrated $BaZrO_3$," *Applied Physics Letters*, vol. 100, no. 6, p. 061903, 2012.

[45] M. J. Scholten, J. Schooman, J. C. van Miltenburg, and H. A. J. Oonk, "Synthesis of strontium and barium cerate and their reaction with carbon dioxide," *Solid State Ionics*, vol. 61, no. 1-3, pp. 83–91, 1993.

[46] M. J. Scholten, J. Schoonman, J. C. van Miltenburg, and E. H. P. Cordfunke, "The thermodynamic properties of $BaCeO_3$ at temperatures from 5 to 940 K," *Thermochimica Acta*, vol. 268, pp. 161–168, 1995.

[47] C. W. Tanner, "Instability of $BaCeO_3$ in H_2O-containing atmospheres," *Journal of The Electrochemical Society*, vol. 143, no. 4, p. 1386, 1996.

[48] H. Iwahara, H. Uchida, and N. Maeda, "High temperature fuel and steam electrolysis cells using proton conductive solid electrolytes," *Journal of Power Sources*, vol. 7, no. 3, pp. 293–301, 1982.

[49] K. D. Kreuer, E. Schonherr, and J. Maier, "Proton and oxygen diffusion in $BaCeO_3$ based compounds: A combined thermal gravimetric analysis and conductivity study," *Solid State Ionics*, vol. 70-71, pp. 278–284, 1994.

[50] E. O. Ahlgren, "Thermoelectric power of $SrCe_{0.95}Y_{0.05}O_{3-\delta}$," *Solid State Ionics*, vol. 97, no. 1-4, pp. 489–495, 1997.

[51] W. Münch, G. Seifert, K.-D. Kreuer, and J. Maier, "A quantum molecular dynamics study of proton conduction phenomena in $BaCeO_3$," *Solid State Ionics*, vol. 86-88, no. 0, pp. 647–652, 1996.

[52] W. Münch, G. Seifert, K.-D. Kreuer, and J. Maier, "A quantum molecular dynamics study of the cubic phase of $BaTiO_3$ and $BaZrO_3$," *Solid State Ionics*, vol. 97, no. 1-4, pp. 39–44, 1997.

[53] M. Pionke, T. Mono, W. Schweika, T. Springer, and H. Schober, "Investigation of the hydrogen mobility in a mixed perovskite: $Ba[Ca_{(1+x)/3}Nb_{(2-x)/3}]O_{3-x/2}$ by quasielastic neutron scattering," *Solid State Ionics*, vol. 97, no. 1-4, pp. 497–504, 1997.

[54] M. Karlsson, M. E. Björketun, P. Sundell, A. Matic, G. Wahnström, D. Engberg, L. Börjesson, I. Ahmed, S.-G. Eriksson, and P. Berastegui, "Vibrational properties of protons in hydrated $BaIn_xZr_{1-x}O_{3-x/2}$," *Physical Review B*, vol. 72, no. 9, p. 094303, 2005.

[55] M. Karlsson, A. Matic, E. Zanghellini, and I. Ahmed, "Temperature-dependent infrared spectroscopy of proton-conducting hydrated perovskite $BaIn_xZr_{1-x}O_{3-x/2}$ (x= 0.10-0.75)," *The Journal of Physical Chemistry C*, vol. 114, no. 13, pp. 6177–6181, 2010.

[56] K.-D. Kreuer, "Aspects of the formation and mobility of protonic charge carriers and the stability of perovskite-type oxides," *Solid State Ionics*, vol. 125, no. 1-4, pp. 285–302, 1999.

[57] M. E. Björketun, P. Sundell, and G. Wahnström, "Effect of acceptor dopants on the proton mobility in $BaZrO_3$: A density functional investigation," *Physical Review B*, vol. 76, no. 5, p. 054307, 2007.

[58] D.-H. Kim, B.-K. Kim, and Y.-C. Kim, "Energy barriers for proton migration in yttrium-doped barium zirconate super cell with $\Sigma 5$ (310)/[001] tilt grain boundary," *Solid State Ionics*, vol. 213, pp. 18–21, 2012.

[59] M. A. Gomez, M. A. Griffin, S. Jindal, K. D. Rule, and V. R. Cooper, "The effect of octahedral tilting on proton binding sites and transition states in pseudo-cubic perovskite oxides," *The Journal of Chemical Physics*, vol. 123, no. 9, p. 094703, 2005.

[60] Q. Zhang, G. Wahnström, M. E. Björketun, S. Gao, and E. Wang, "Path integral treatment of proton transport processes in $BaZrO_3$," *Physical Review Letters*, vol. 101, no. November, pp. 1–4, 2008.

[61] P. Raiteri, J. D. Gale, and G. Bussi, "Reactive force field simulation of proton diffusion in $BaZrO_3$ using an empirical valence bond approach," *Journal of Physics. Condensed matter : an Institute of Physics journal*, vol. 23, no. 33, p. 334213, 2011.

[62] B. Groß, C. Beck, F. Meyer, T. Krajewski, R. Hempelmann, and H. Altgeld, "$BaZr_{0.85}Me_{0.15}O_{2.925}$ (Me=Y, In and Ga): Crystal growth, high-resolution transmission electron microscopy, high-temperature X-ray diffraction and neutron scattering experiments," *Solid State Ionics*, vol. 145, no. 1-4, pp. 325–331, 2001.

[63] C. Beck, S. Janssen, B. Groß, and R. Hempelmann, "Neutron time-of-flight spectrometer FOCUS at SINQ: Results from nanocrystalline matter studies," *Scripta Materialia*, vol. 44, no. 8-9, pp. 2309–2313, 2001.

[64] A. K. Azad, C. Savaniu, S. Tao, S. Duval, P. Holtappels, R. M. Ibberson, and J. T. S. Irvine, "Structural origins of the differing grain conductivity values in $BaZr_{0.9}Y_{0.1}O_{2.95}$ and indication of novel approach to counter defect association," *Journal of Materials Chemistry*, vol. 18, no. 29, p. 3414, 2008.

[65] P. Colomban, O. Zaafrani, and A. Slodczyk, "Proton content and nature in perovskite ceramic membranes for medium temperature fuel cells and electrolysers," *Membranes*, vol. 2, no. 3, pp. 493–509, 2012.

[66] N. Jalarvo, L. Stingaciu, D. Gout, Z. Bi, M. P. Paranthaman, and M. Ohl, "Proton dynamics in $La_{0.8}Ba_{1.2}GaO_{3.9} \cdot nH_2O$ studied by quasielastic incoherent neutron scattering," *Solid State Ionics*, vol. 252, pp. 12–18, 2013.

[67] M. Karlsson, "Proton dynamics in oxides: Insight into the mechanics of proton conduction from quasielastic neutron scattering," *Physical Chemistry Chemical Physics*, vol. 17, no. 1, pp. 26–38, 2015.

[68] C. Karmonik, R. Hempeimann, J. Cook, F. Güthoff, U. Saarlandes, and L. Langevin, "Investigation of the proton migration mechanism in the perovskite proton conductor $Ba_3Ca_{1.18}Nb_{1.822}H_{0.2}O_{8.83}$ by means of quasielastic neutron scattering," *Ionics*, vol. 2, pp. 69–74, 1996.

[69] T. Matzke, U. Stimming, C. Karmonik, M. Soetratmo, R. Hempelmann, and F. Guthoff, "Quasielastic thermal neutron scattering experiment on the proton conductor $SrCe_{0.95}Yb_{0.05}H_{0.02}O_{2.985}$," *Solid State Ionics*, vol. 88, no. 96, pp. 621–628, 1996.

[70] M. Karlsson, A. Matic, D. Engberg, M. E. Björketun, M. M. Koza, I. Ahmed, G. Wahnström, L. Börjesson, and S.-G. Eriksson, "Quasielastic neutron scattering of hydrated $BaZr_{0.90}A_{0.10}O_{2.95}$ (A=Y and Sc)," *Solid State Ionics*, vol. 180, no. 1, pp. 22–28, 2009.

[71] D. Wilmer, T. Seydel, and K.-D. Kreuer, "Proton diffusion in hydrated acceptor-doped barium zirconate," *MRS Proceedings*, vol. 972, pp. 0972–AA01–04, 2006.

[72] P. Colomban and A. Slodczyk, "Proton dynamics and structural modifications in the protonic conductor perovskites," *Journal of the Physical Society of Japan*, vol. 79, no. Suppl A, pp. 1–6, 2010.

[73] R. Hempelmann, C. Karmonik, T. Matzke, M. Cappadonia, U. Stimming, T. Springer, and M. A. Adams, "Quasielastic neutron scattering study of proton diffusion in $SrCe_{0.95}Yb_{0.05}H_{0.02}O_{2.985}$," *Solid State Ionics*, vol. 77, no. 94, pp. 152–156, 1995.

[74] N. Sata, S. Shin, K. Shibata, and M. Ishigame, "Proton diffusion in $SrZr_{0.95}Y_{0.05}O_3$ observed by quasielastic neutron scattering," *Journal of the Physical Society of Japan*, vol. 68, no. 11, pp. 3600–3602, 1999.

[75] A. Braun, S. Duval, P. Ried, and J. Embs, "Proton diffusivity in the $BaZr_{0.9}Y_{0.1}O_{3-\delta}$ proton conductor," *Journal of Applied Electrochemistry*, vol. 39, no. 4, pp. 471–475, 2009.

[76] M. Karlsson, D. Engberg, M. E. Björketun, A. Matic, G. Wahnström, P. G. Sundell, P. Berastegui, I. Ahmed, P. Falus, B. Farago, L. Börjesson, and S.-G. Eriksson, "Using neutron spin-echo to investigate proton dynamics in proton-conducting perovskites," *Chemistry of Materials*, vol. 22, no. 3, pp. 740–742, 2010.

[77] Q. Chen, J. Banyte, X. Zhang, J. P. Embs, and A. Braun, "Proton diffusivity in spark plasma sintered $BaCe_{0.8}Y_{0.2}O_{3-\delta}$: In-situ combination of quasi-elastic neutron scattering and impedance spectroscopy," *Solid State Ionics*, vol. 252, pp. 2–6, 2013.

[78] A. Braun and Q. Chen, "Experimental neutron scattering evidence for proton polaron in hydrated metal oxide proton conductors," *Nature Communications*, vol. 8, no. May, pp. 1–8, 2017.

[79] C. T. Chudley and R. J. Elliott, "Neutron scattering from a liquid on a jump diffusion model," *Proceedings of the Physical Society*, vol. 77, no. 2, pp. 353–361, 1961.

[80] A. L. Samgin, "Doping effects on protonic conduction in $SrCeO_3$- and $BaCeO_3$-based perovskites," *Inorganic Materials*, vol. 36, no. 8, pp. 979–982, 2000.

[81] M. S. Islam, R. A. Davies, and J. D. Gale, "Proton migration and defect interactions in the $CaZrO_3$ orthorhombic perovskite: A quantum mechanical study," *Chemistry of Materials*, vol. 13, no. 6, pp. 2049–2055, 2001.

[82] M. Gomez, M. Chunduru, L. Chigweshe, L. Foster, S. J. Fensin, K. M. Fletcher, and L. E. Fernandez, "The effect of yttrium dopant on the proton conduction pathways of $BaZrO_3$, a cubic perovskite," *The Journal of Chemical Physics*, vol. 132, no. 21, p. 214709, 2010.

[83] M. S. Islam, R. A. Davies, and J. D. Gale, "Hop, skip or jump? proton transport in the $CaZrO_3$ perovskite oxide," *Chemical Communications*, vol. 3, no. 7, pp. 661–662, 2001.

[84] M. Karlsson, A. Matic, C. S. Knee, I. Ahmed, S.-G. Eriksson, and L. Börjesson, "Short-range structure of proton-conducting perovskite $BaIn_xZr_{1-x}O_{(3-x/2)}$ (x = 0-0.75)," *Chemistry of Materials*, vol. 20, no. 10, pp. 3480–3486, 2008.

[85] M. Karlsson, A. Matic, S. F. Parker, I. Ahmed, L. Börjesson, and S. Eriksson, "O-H wag vibrations in hydrated $BaIn_xZr_{1-x}O_{3-x/2}$ investigated with inelastic neutron scattering," *Physical Review B*, vol. 77, no. 10, p. 104302, 2008.

[86] K.-D. Kreuer, S. Adams, W. Münch, A. Fuchs, U. Klock, and J. Maier, "Proton conducting alkaline earth zirconates and titanates for high drain electrochemical applications," *Solid State Ionics*, vol. 145, no. 1-4, pp. 295–306, 2001.

[87] F. Giannici, A. Longo, K.-D. Kreuer, A. Balerna, and A. Martorana, "Dopants and defects: Local structure and dynamics in barium cerates and zirconates," *Solid State Ionics*, vol. 181, no. 3-4, pp. 122–125, 2010.

[88] F. Giannici, A. Longo, A. Balerna, K.-D. Kreuer, and A. Martorana, "Proton dynamics in In:$BaZrO_3$: Insights on the atomic and electronic structure from X-ray absorption spectroscopy," *Chemistry of Materials*, vol. 21, no. 13, pp. 2641–2649, 2009.

[89] M. Karlsson, I. Ahmed, A. Matic, and S.-G. Eriksson, "Short-range structure of proton-conducting $BaM_{0.10}Zr_{0.90}O_{2.95}$ (M=Y, In, Sc and Ga) investigated with vibrational spectroscopy," *Solid State Ionics*, vol. 181, no. 3-4, pp. 126–129, 2010.

[90] M. A. Gomez, G. Kwan, W. Zhu, M. Chelliah, X. Zuo, A. Eshun, V. Blackmer, T. Huynh, and M. Huynh, "Ordered yttrium concentration effects on barium zirconate structure, proton binding sites and transition states," *Solid State Ionics*, vol. 304, pp. 126–134, 2017.

[91] A. Longo, F. Giannici, A. Balerna, C. Ingrao, F. Deganello, and M. Antonino, "Local environment of yttrium in Y-doped barium cerate compounds," *Chemistry of Materials*, vol. 18, no. 24, pp. 5782–5788, 2006.

[92] R. Hempelmann, "Hydrogen diffusion mechanism in proton conducting oxides," *Physica B: Condensed Matter*, vol. 226, no. 1-3, pp. 72–77, 1996.

[93] R. Hempelmann, M. Soetratmo, O. Hartmann, and R. Wäppling, "Muon diffusion and trapping in proton conducting oxides," *Solid State Ionics*, vol. 107, no. 3-4, pp. 269–280, 1998.

[94] Y. Yamazaki, F. Blanc, Y. Okuyama, L. Buannic, J. C. Lucio-Vega, C. P. Grey, and S. M. Haile, "Proton trapping in yttrium-doped barium zirconate," *Nature materials*, vol. 12, no. 7, pp. 647–651, 2013.

[95] M. E. Björketun, P. Sundell, G. Wahnström, and D. Engberg, "A kinetic Monte Carlo study of proton diffusion in disordered perovskite structured lattices based on first-principles calculations," *Solid State Ionics*, vol. 176, no. 39-40, pp. 3035–3040, 2005.

[96] P. G. Sundell, M. E. Björketun, and G. Wahnström, "Density-functional calculations of prefactors and activation energies for H diffusion in $BaZrO_3$," *Physical Review B*, vol. 76, no. 9, p. 094301, 2007.

[97] M. S. Islam, P. R. Slater, J. R. Tolchard, and T. Dinges, "Doping and defect association in $AZrO_3$ (A = Ca, Ba) and LaMO_3 (M = Sc, Ga) perovskite-type ionic conductors.," *Dalton Transactions*, vol. 3, no. 19, pp. 3061–6, 2004.

[98] N. Kitamura, J. Akola, S. Kohara, K. Fujimoto, and Y. Idemoto, "Proton distribution and dynamics in Y and Zn doped $BaZrO_3$," *The Journal of Physical Chemistry C*, vol. 118, pp. 18846–18852, 2014.

[99] P. Haro-González, M. Karlsson, S. M. Gaita, C. S. Knee, and M. Bettinelli, "Eu^{3+} as a luminescent probe for the local structure of trivalent dopant ions in barium zirconate-based proton conductors," *Solid State Ionics*, vol. 247-248, pp. 94–97, 2013.

[100] K.-D. Kreuer, "On the development of proton conducting materials for technological applications," *Solid State Ionics*, vol. 97, no. 1-4, pp. 1–15, 1997.

[101] D. Zeudmi Sahraoui and T. Mineva, "Effect of dopant nature on structures and lattice dynamics of proton-conducting $BaZrO_3$," *Solid State Ionics*, vol. 253, pp. 195–200, 2013.

[102] F. Giannici, A. Longo, A. Balerna, K.-D. Kreuer, and A. Martorana, "Indium doping in barium cerate: The relation between local symmetry and the formation and mobility of protonic defects," *Chemistry of Materials*, vol. 19, no. 23, pp. 5714–5720, 2007.

[103] D. Han, N. Hatada, T. Uda, and R. Koc, "Chemical expansion of yttrium-doped barium zirconate and correlation with proton concentration and conductivity," *Journal of the American Ceramic Society*, vol. 99, no. 11, pp. 3745–3753, 2016.

[104] M. Karlsson, P. Fouquet, I. Ahmed, and M. Maccarini, "Dopant concentration and short-range structure dependence of diffusional proton dynamics in hydrated $BaIn_xZr_{1-x}O_{3-x/2}$ ($x = 0.10$ and 0.50)," *The Journal of Physical Chemistry C*, vol. 114, no. 7, pp. 3292–3296, 2010.

[105] I. Ahmed, S.-G. Eriksson, E. Ahlberg, C. S. Knee, P. Berastegui, L. G. Johansson, H. Rundlöf, M. Karlsson, A. Matic, L. Börjesson, and D. Engberg, "Synthesis and structural characterization of perovskite type proton conducting $BaZr_{1-x}In_xO_{3-x}$," *Solid State Ionics*, vol. 177, no. 17-18, pp. 1395–1403, 2006.

[106] S. W. Lovesey, *Theory of Neutron Scattering from Condensed Matter*. London: Oxford University Press, 1984.

[107] G. L. Squires, *Introduction to the Theory of Thermal Neutron Scattering*. Courier Corporation, 1978.

[108] H. Schober, "Diffusion des neutrons par la matière cristalline ou amorphe non-magnétique," *École thématique de la Société Française de la Neutronique*, vol. 10, pp. 159–336, 2010.

[109] A. Messiah, *Quantum Mechanics, Volume I*. Amsterdam, The Netherlands: North-Holland Publishing Company, 1967.

[110] B. N. Brockhouse, "Slow neutron spectroscopy and the grand atlas of the physical world," *Reviews of Modern Physics*, vol. 67, no. 4, pp. 735–751, 1995.

[111] L. van Hove, "Correlations in space and time and Born approximation scattering in systems of interacting particles," *Physical Review*, vol. 95, no. 1, pp. 249–262, 1954.

[112] V. F. Sears, "Neutron scattering lengths and cross sections," *Neutron News*, vol. 3, no. 3, pp. 26–37, 1992.

[113] M. Bée, *Quasielastic Neutron Scattering: Principles and Applications in Solid State Chemistry, Biology and Materials Science*. Bristol and Philadelphia: Adam Hilger, 1988.

[114] S. Yip, "Quasi-elastic scattering in neutron and laser spectroscopy," in *Spectroscopy in biology and chemistry: neutrons, Xray, laser* (S.-H. Chen and S. Yip, eds.), Academic Press, 1974.

[115] R. M. Moon, T. Riste, and W. C. Koehler, "Polarization analysis of thermal-neutron scattering," *Physical Review*, vol. 181, no. 2, pp. 920–931, 1969.

[116] P. Gerlach, O. Schärpf, W. Prandl, and B. Dorner, "Separation of the coherent and incoherent scattering of C_2Cl_6 by polarization analysis," *Journal de Physique*, vol. 43, no. 12, pp. C7–151, 1982.

[117] O. Schärpf and H. Capellmann, "The xyz-difference method with polarized neutrons and the separation of coherent, spin incoherent, and magnetic scattering cross sections in a multidetector," *Physica Status Solidi (a)*, vol. 135, no. 2, pp. 359–379, 1993.

[118] J. R. Stewart, P. P. Deen, K. H. Andersen, H. Schober, J.-F. Barthélémy, J. M. Hillier, A. P. Murani, T. Hayes, and B. Lindenau, "Disordered materials studied using neutron polarization analysis on the multi-detector spectrometer, D7," *Journal of Applied Crystallography*, vol. 42, no. 1, pp. 69–84, 2008.

[119] S. Peggs, R. Kreier, C. Carlile, ..., and J. Yeck, eds., *ESS Technical Design Report*. 2013.

[120] H. Schober, "Neutron scattering instrumentation," in *Neutron Applications in Earth, Energy and Environmental Sciences* (L. Liang, R. Rinaldi, and H. Schober, eds.), pp. 37–104, Boston, MA: Springer US, 2009.

[121] T. Brückel, G. Heger, R. Zorn, and D. Richter, *Neutron Scattering : Lectures of the JCNS Laboratory Course Held at Forschungszentrum Jülich and the Research Reactor FRM II of TU Munich ; in Cooperation with RWTH Aachen and University of Münster*. Forschungszentrum, Zentralbibliothek, 2008.

[122] J. Ollivier and J.-M. Zanotti, "Diffusion inélastique de neutrons par temps de vol," *JDN 16 - Diffusion Inélastique des Neutrons pour l'Etude des Excitations dans la Matiére Condensée*, vol. 10, pp. 379–423, 2010.

[123] B. Frick, "Neutron backscattering spectroscopy," in *Neutron and X-ray Spectroscopy*, pp. 483–527, Berlin/Heidelberg: Springer-Verlag, 2006.

[124] "http://www.ill.eu."

[125] M. A. Appel, *Ring Rotation in Ferrocene and Ferrocene-containing Polymers*. PhD thesis, Technische Universität, Darmstadt, 2015.

[126] B. Frick, J. Combet, and L. Van Eijck, "New possibilities with inelastic fixed window scans and linear motor Doppler drives on high resolution neutron backscattering spectrometers," *Nuclear Instruments and Methods in Physics Research, Section A: Accelerators, Spectrometers, Detectors and Associated Equipment*, vol. 669, pp. 7–13, 2012.

[127] "https://neutrons.ornl.gov/basis."

[128] B. Farago, "The basics of neutron spin echo," in *Neutron Data Booklet* (A.-J. Dianoux and G. Lander, eds.), OCP Science, second edi ed., 2003.

[129] F. Mezei, "Neutron spin echo: A new concept in polarized thermal neutron techniques," *Zeitschrift für Physik*, vol. 255, no. 2, pp. 146–160, 1972.

[130] F. Mezei, C. Pappas, and T. Gutberlet, eds., *Neutron Spin Echo Spectroscopy*, vol. 601 of *Lecture Notes in Physics*. Berlin, Heidelberg: Springer Berlin Heidelberg, 2003.

[131] I. Ahmed, C. S. Knee, M. Karlsson, S.-G. Eriksson, P. F. Henry, A. Matic, D. Engberg, and L. Börjesson, "Location of deuteron sites in the proton conducting perovskite $BaZr_{0.50}In_{0.50}O_{3-y}$," *Journal of Alloys and Compounds*, vol. 450, pp. 103–110, 2008.

[132] J. D. Barnes, "Inelastic neutron scattering study of the "rotator" phase transition in n-nonadecane," *The Journal of Chemical Physics*, vol. 58, no. 12, p. 5193, 1973.

[133] A. J. Dianoux, F. Volino, and H. Hervet, "Incoherent scattering law for neutron quasi-elastic scattering in liquid crystals," *Molecular Physics*, no. August 2014, pp. 37–41, 1975.

[134] R. E. Lechner, G. Badurek, A. J. Dianoux, H. Hervet, and F. Volino, "On the rotational motion of the ammonium ion in the CsCl-type phase of NH_4Br: Results from quasielastic neutron scattering," *The Journal of Chemical Physics*, vol. 73, no. 2, p. 934, 1980.

[135] F. Volino and A. J. Dianoux, "Neutron incoherent scattering law for diffusion in a potential of spherical symmetry: General formalism and application to diffusion inside a sphere," *Molecular Physics*, vol. 41, no. 2, pp. 271–279, 1980.

[136] I. Ahmed, M. Karlsson, S.-G. Eriksson, E. Ahlberg, C. S. Knee, K. Larsson, A. K. Azad, A. Matic, and L. Börjesson, "Crystal structure and proton conductivity of $BaZr_{0.9}Sc_{0.1}O_{3-\delta}$," *Journal of the American Ceramic Society*, vol. 91, no. 9, pp. 3039–3044, 2008.

[137] F. Giannici, M. Shirpour, A. Longo, A. Martorana, R. Merkle, and J. Maier, "Long-range and short-range structure of proton-conducting Y:$BaZrO_3$," *Chemistry of Materials*, vol. 23, no. 11, pp. 2994–3002, 2011.

[138] P. L. Hall and D. K. Ross, "Incoherent neutron scattering functions for random jump diffusion in bounded and infinite media," *Molecular Physics*, vol. 42, no. 3, pp. 673–682, 1981.

[139] K. S. Singwi and A. Sjölander, "Diffusive motions in water and cold neutron scattering," *Physical Review*, vol. 119, no. 3, pp. 863–871, 1960.

[140] K. Kuhlmann, *Development and Commissioning of a Prototype Neutron Backscattering Spectrometer with an Energy Resolution Enhanced by an*

Order of Magnitude Using GaAs Single Crystals. PhD thesis, Friedrich-Alexander-Universität Erlangen-Nürnberg (FAU), 2018.

[141] A. Al-Wahish, D. Armitage, U. Al-Binni, B. Hill, R. Mills, N. Jalarvo, L. Santodonato, K. W. Herwing, and D. Mandrus, "A new apparatus design for high temperature (up to 950 °C) quasi-elastic neutron scattering in a controlled gaseous environment," *Review of Scientific Instruments*, no. 86, p. 095102, 2015.

[142] D. A. Mc Quarrie and J. D. Simon, *Physical Chemistry. A Molecular Approach.* Sausalito: University Science Books, 1997.

[143] I. Ahmed, F. G. Kinyanjui, S. M. H. Rahman, P. Steegstra, S. G. Eriksson, and E. Ahlberg, "Proton conductivity in mixed B-site doped perovskite oxide $BaZr_{0.5}In_{0.25}Yb_{0.25}O_{3-\delta}$," *Journal of The Electrochemical Society*, vol. 157, no. 12, p. B1819, 2010.